Summer 8-2019

The Axisymmetric Harmonic Element Including Gyroscopic Effects: A Complete Derivation

Zachary Charles Glick

The Axisymmetric Harmonic Element Including Gyroscopic Effects: A Complete Derivation

A Thesis

Submitted to the Faculty

of

Rose-Hulman Institute of Technology

by

Zachary Charles Glick

In Partial Fulfillment of the Requirements for the Degree

of

Master of Science in Mechanical Engineering

August 2019

ROSE-HULMAN INSTITUTE OF TECHNOLOGY

Final Examination Report

Zachary Glick — Name

Mechanical Engineering — Graduate Major

Thesis Title: The Axisymmetric Harmonic Element Including Gyroscopic Effects: A Complete Derivation

DATE OF EXAM: August 26, 2019

EXAMINATION COMMITTEE:

	Thesis Advisory Committee	Department
Thesis Advisor:	Simon Jones	ME
	Lorranie Olson	ME
	Joseph Eichholz	MA

PASSED X **FAILED** _____

ABSTRACT

Glick, Zachary Charles

M.S.M.E.

Rose-Hulman Institute of Technology

August 2019

The Axisymmetric Harmonic Element Including Gyroscopic Effects: A Complete Derivation

Thesis Advisor: Dr. Simon Jones

Various types of finite elements have been used in the prediction of critical speeds of turbomachinery. Among these, axisymmetric harmonic elements provide both accurate natural frequency prediction and computational speed. Yet, a full derivation of such an element including gyroscopic effects is not widely available in the relevant literature.

In this work, the finite elements for rotordynamics available in the literature are reviewed. Derivations necessary for the axisymmetric harmonic element mass, gyroscopic damping, and stiffness matrices and the equations of motion are clearly expounded using Hamilton's principle.

The formulation is applied to two model shafts, and the comparison of results is documented showing the axisymmetric harmonic element to be adequate for use in critical speed identification. Rotor natural frequencies and mode shapes are yielded from the quadratic eigenvalue problem. The generation of Campbell diagrams, made available by the inclusion of gyroscopic effects, is performed.

Key Words: Mechanical Engineering, finite element, gyroscopic matrix

DEDICATION

Domino et Deo meo, Deo et Omni meo.

ACKNOWLEDGEMENTS

A special note of gratitude to Dr. Simon Jones, whose direction and guidance made this project possible. Thank you to my parents and family whose support always encourages me.

TABLE OF CONTENTS

Contents

LIST OF FIGURES

Figure Page

LIST OF TABLES

Table Page

LIST OF ABBREVIATIONS

DOF	degree(s) of freedom
Hz	Hertz
MAC	Modal Assurance Criterion
rad	radians
rpm	revolutions per minute

LIST OF SYMBOLS

Latin Symbols

a	one-half element width
b	one-half element height
c	elemental gyroscopic damping matrix, coordinate vector at a point, stress-strain matrix constant
d	nodal displacement vector
j	indexing variable
k	elemental stiffness matrix, indexing variable
m	elemental mass matrix, diagonal of the mass matrix
n	number of nodal waves, number of Gauss points
p	Gauss point
r	radial coordinate, radius
s	horizontal isoparametric coordinate, real part of eigenvalue solution vector (stability)
t	vertical isoparametric coordinate
u	displacement vector at a point, radial displacement, mode shape vector
v	circumferential displacement
w	axial displacement, Gauss weight
x	a Cartesian coordinate
y	a Cartesian coordinate
z	axial coordinate
A	quadratic eigenvalue problem input matrix
B	quadratic eigenvalue problem input matrix
C	gyroscopic damping matrix, elemental gyroscopic damping matrix integrand
D	global displacement vector
E	stress-strain relationship matrix, Young's modulus
F	force vector
G	shear modulus
I	identity matrix
J	Jacobian matrix
K	global stiffness matrix
L	shaft length, Lagrangian
M	global mass matrix, total number of nodes in model
N	shape function matrix, number of nodes per element
T	kinetic energy
U	potential energy, strain energy
V	external work, volume

Greek Symbols

γ	shear strain
ε	strain vector, strain

θ	circumferential coordinate
λ	imaginary part of eigenvalue solution vector
ν	Poisson's ratio
π	mathematical constant, ratio of circle circumference to its diameter
ρ	material density
σ	stress vector
τ	shear stress
ϕ	an arbitrary function
ψ	eigenvector solution matrix
Λ	quadratic eigenvalue problem eigenvalue solution vector
Ψ	quadratic eigenvalue problem eigenvector solution matrix
Ω	axial rotation speed

Mathematical Symbols

d	differential
i	imaginary number ($\sqrt{-1}$)
∂	partial derivative, operator matrix
[]	matrix
{}	column vector
$\dot{}$	first time derivative
$\ddot{}$	second time derivative
Σ	summation
$\bar{}$	symmetric with respect to origin of circumferential coordinate
$=$	antisymmetric with respect to origin of circumferential coordinate
^{T}	transpose
$\int$	integral
$\lvert\ \rvert$	determinant, absolute value

GLOSSARY

Axisymmetry - a special type of rotational symmetry where a one or two-dimensional shape is rotated 360 degrees about a central axis.

Campbell diagram - a graph with operating speed plotted on the horizontal axis and frequency plotted on the vertical axis.

Hertz - the SI unit of frequency, equal to one cycle per second.

Mode shape - the shape of the deformed structure if it is excited by a dynamic force which has the same frequency as the natural frequency of the structure. The mode shape has no unit.

Natural frequency - the frequency at which a system oscillates when not subjected to a continuous or repeated external force.

Rotor Whirl - the rotor's bulk precession about its undeflected axis

1 INTRODUCTION

1.1. Background and Definition of Terms

In the field of structural dynamics, the vibration of rotating machinery has been of particular interest in the past several decades due to the increased use of such machinery necessitating a greater ability to analyze their vibrational characteristics for the purpose of safety. Rotating machinery is commonly used in energy production such as in civil energy generation as well as in aircraft and marine engines. These applications are commonly tested in a physical experimental setting preceded by testing using computer simulations (*i.e.,* finite elements analyses). A finite element modal analysis computes the natural frequencies and their associated mode shapes.

The field of rotordynamics studies the dynamic behavior of rotor structures such as that of a gas-turbine engine. Figure 1.1 shows a schematic diagram of a simple rotor structure—a shaft with one disk.

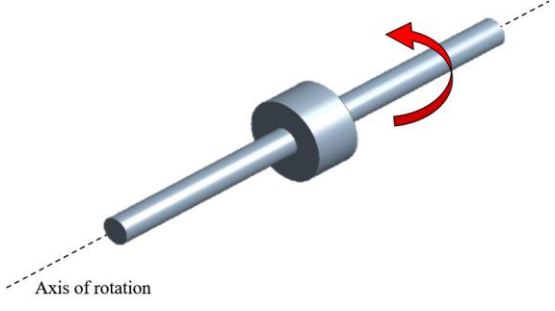

Figure 1.1: Schematic diagram of rotating shaft with disk

Common types of rotors to analyze include the high- and low-pressure shafts of an axial-flow gas turbine engine. The low-pressure shaft consists of a low-pressure compressor (and fan if the

engine type is turbofan) and turbine. The high-pressure shaft includes the high-pressure compressor and turbine. Figure 1.2 shows a schematic diagram of a turbofan and of its high-pressure shaft.

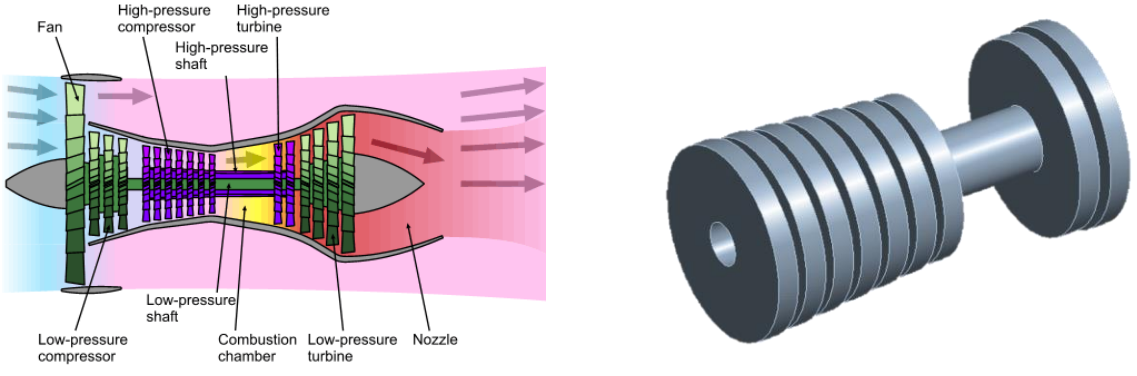

(a) **(b)**

Figure 1.2: Schematic diagram: (a) turbofan, (b) high-pressure shaft [1]

As shown by Figure 1.2.b, a solid disk on a shaft can represent a bladed disk, such as a rotor in a multi-stage compressor or turbine.

Mode shapes of a rotor are shown in Figure 1.3. Mode shapes where the shaft displays a bend along its axial direction are called bend modes and are of interest when analyzing the design of a rotating structure.

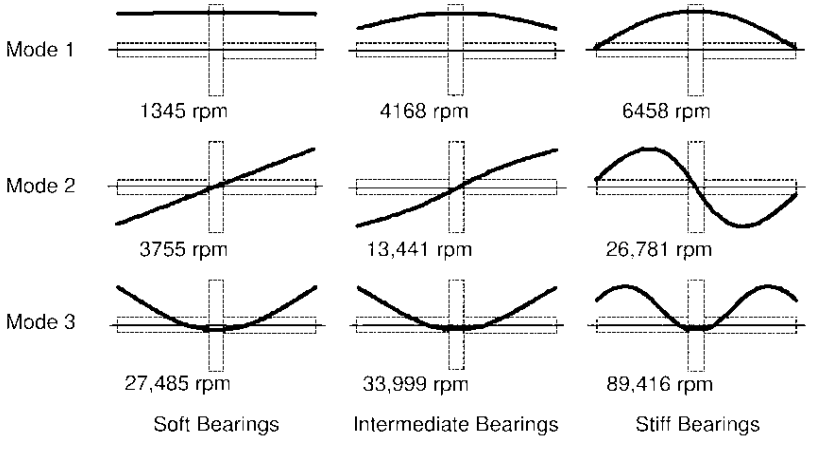

Figure 1.3: First three mode shapes for three different bearing stiffness's [2]

Rotors are often geometrically axisymmetric in design. Axisymmetry describes the set of conditions in which geometry, loading, and constraints in a planar area are symmetric about an axis parallel to that plane. In a purely axisymmetric analysis, there is no variation with respect to the circumferential coordinate. However, nodal waves need to be taken into account in order to describe the dynamic behavior of a rotor. Nodal waves are described in Figure 1.4.

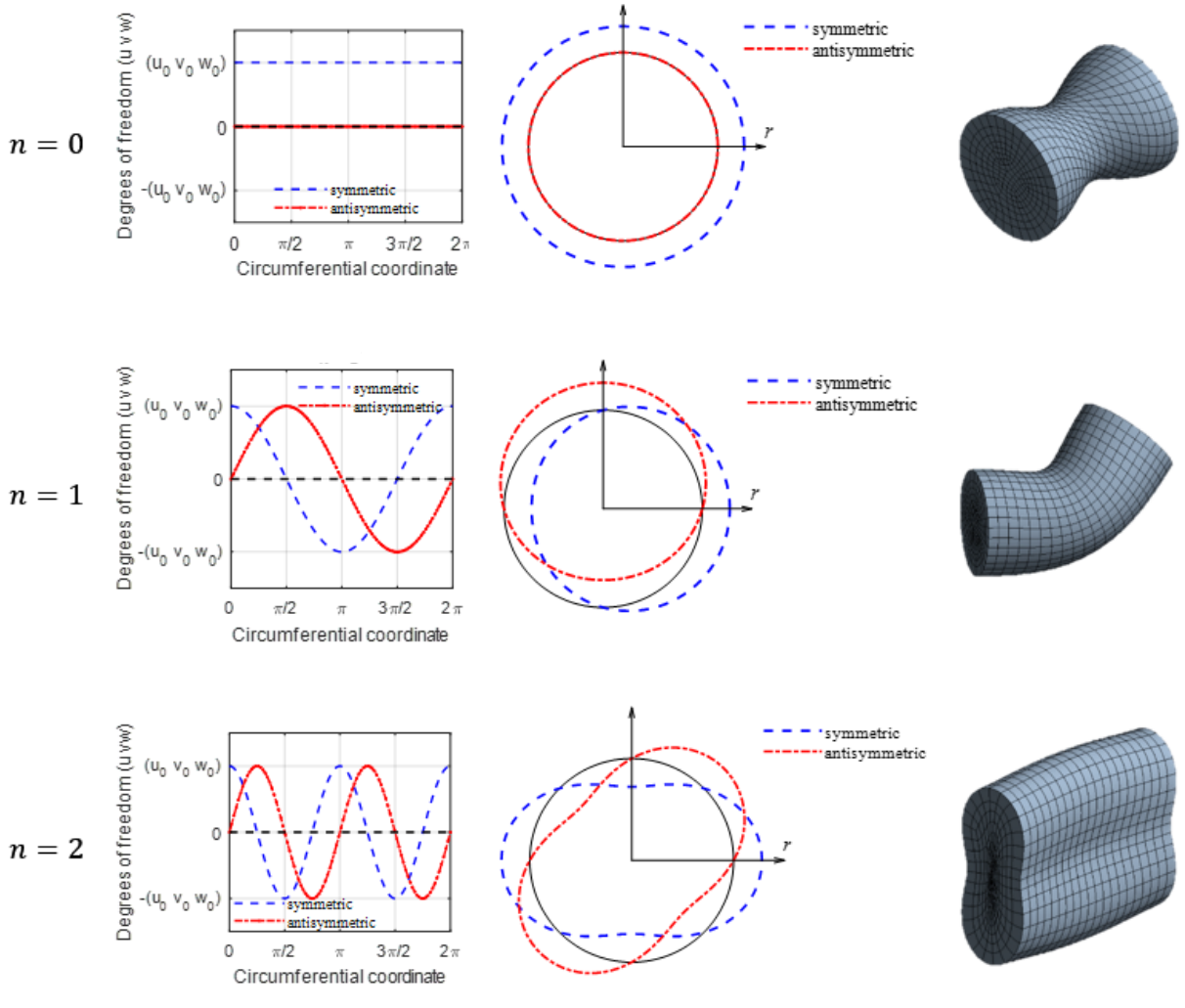

Figure 1.4: Visualization of nodal wave number

Because of the axisymmetric nature of rotors, it is convenient to describe them using cylindrical coordinates r (radial), θ (circumferential), and z (axial). Cylindrical coordinates are graphically depicted in Figure 1.5.

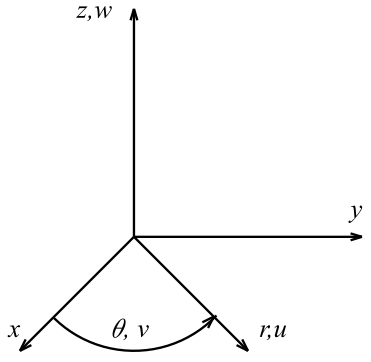

Figure 1.5: Cylindrical coordinate system

Coordinates are transformed from cylindrical to Cartesian and vice versa using Equations 1.1.

$$x = r\,cos(\theta) \quad 1.1a$$

$$y = r\,sin(\theta) \quad 1.1b$$

$$z = z \quad 1.1c$$

$$r = \sqrt{x^2 + y^2} \quad 1.1d$$

$$\theta = \tan^{-1}\left(\frac{y}{x}\right) \quad 1.1e$$

Figure 1.6 shows the relationship between the displacement degrees of freedom in the $r - \theta$ plane and those in the $x - y$ plane.

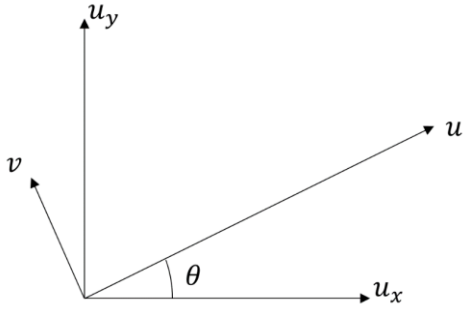

Figure 1.6: Relationship between DOF in the $r - \theta$ plane and those in the $x - y$ plane

Degrees of freedom in the $x - y$ plane are calculated from those in the $r - \theta$ plane using Equations 1.2, and degrees of freedom in the $r - \theta$ plane are calculated from those in the $x - y$ plane using Equations 1.3.

$$u_x = u\,cos(\theta) - v\,sin(\theta) \quad \text{1.2a}$$

$$u_y = u\,sin(\theta) + v\,cos(\theta) \quad \text{1.2b}$$

$$u = u_x\,cos(\theta) + u_y\,sin(\theta) \quad \text{1.3a}$$

$$v = -u_x\,sin(\theta) + u_y\,cos(\theta) \quad \text{1.3b}$$

Since rotor systems are often used in machines such as aircraft engines where the operating speed varies over time, Campbell diagrams are used to illustrate how natural frequencies vary at different operating speeds. A Campbell diagram plots the natural frequencies over a wide shaft operating speed range [2]. Figure 1.7 shows a Campbell diagram produced by commercial finite element software.

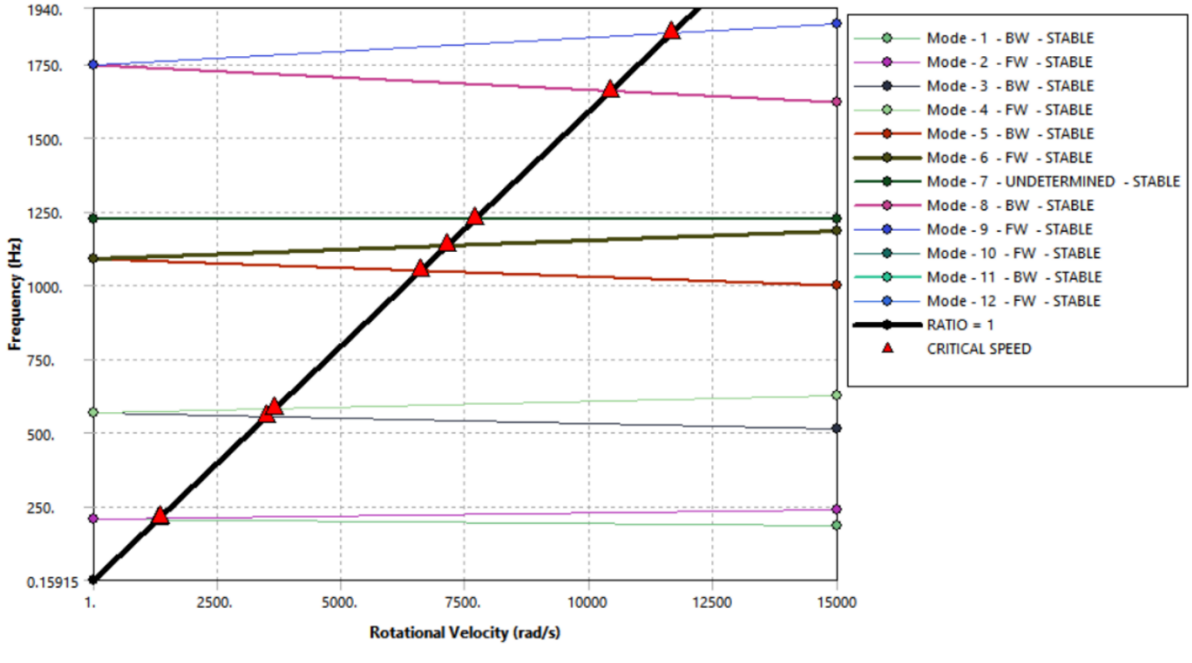

Figure 1.7: Campbell diagram produced from commercial finite element software

The Campbell diagram shows that forward whirl (FW) and backward whirl (BW) mode shapes for a specific natural frequency diverge as the rotor's operating speed increases. In forward whirl, the shaft spins in the same direction as the whirl. In backward whirl, the shaft spins in the opposite direction as the whirl. The difference between forward and backward whirl is shown in Figure 1.8.

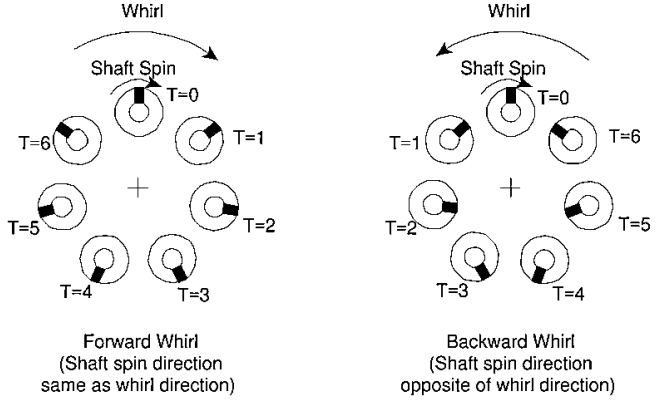

Figure 1.8: Forward and backward whirl [2]

1.2. Brief Summary of Literature, Advantages and Disadvantages, and Need For Present Work

Early finite elements formulations such as that of Nelson, H.D., and McVaugh, J.M. [3] do not require great computational resources, but are limited in their ability to accurately predict natural frequencies. These elements are especially limited in their ability to predict natural frequencies of more complex rotor systems. Three-dimensional solid elements are also available for use. These elements give accurate predictions of mode shapes and natural frequencies, but they require greater computational resources. An element formulation such as the harmonic axisymmetric method of Geradin and Kill [4] provides adequate accuracy of prediction of natural frequencies and is also computationally efficient as it essentially reduces the computation from three to two-dimensions while maintaining the ability to express the variation of the shaft in the circumferential direction unlike purely axisymmetric models or beam models.

Although a vast amount of literature exists in this field, a work is not commonly available which clearly and thoroughly presents each step of all the procedures in the derivation required to perform the vibrational analysis of rotating axisymmetric structures, including gyroscopic effects. Secondly, because of the nature of engineering research, the current literature assumes a level of proficiency in computational methods of structural dynamics. This makes a portion of the current research largely inaccessible to engineers having only an introductory level of knowledge in this particular branch of structural dynamics. Therefore, a work is necessary which gives a clear and comprehensive presentation of all the steps of the finite element derivation for the modal analysis of a rotating axisymmetric structure, including gyroscopic effects, bridging the gap between derivations of varying authorship, while at the same time, making this method accessible to engineers having an introductory level of understanding in this branch of computational methods for structural dynamics.

1.3. Research Hypothesis, Objectives, and Questions; Outline of Structure and Methodology

The present work examines the hypothesis that axisymmetric harmonic elements provide an accurate computation of natural frequencies and mode shapes and are less computationally demanding than full 3D models and that their implementation is available to engineers of advancing expertise in computational methods for structural dynamics. This work derives the mass, gyroscopic damping, and stiffness matrices and the dynamic equations of motion for axisymmetric harmonic finite elements using cylindrical coordinates. The gyroscopic damping matrix takes into account the kinetic energy due to gyroscopic effects. This matrix couples the bending of the shaft in the two orthogonal directions perpendicular to the shaft axis. The axisymmetric harmonic element uses a Fourier series expansion in the circumferential direction to describe displacements which are symmetric and antisymmetric with respect to the origin of

the circumferential coordinate. Displacements that are symmetric and antisymmetric with respect to the circumferential coordinate are described in Figure 1.9 with Equations 1.4.

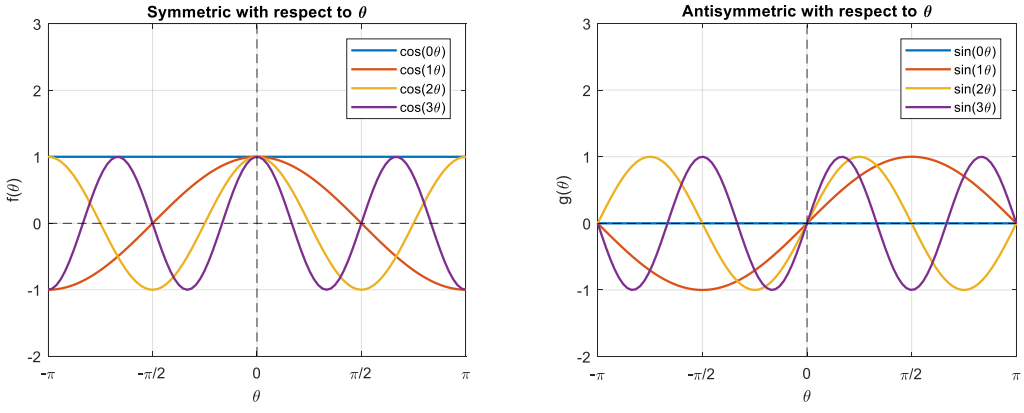

Figure 1.9: Symmetric and antisymmetric functions

	Function	Example	
Symmetric	$f(-x) = f(x)$	$\cos(-n\theta) = \cos(n\theta)$	1.4a
Antisymmetric	$g(-x) = -g(x)$	$\sin(-n\theta) = -\sin(n\theta)$	1.4b

Element matrices are calculated by mapping the elements in cylindrical coordinates to isoparametric coordinates, and Gaussian integration is employed.

The dynamic equations of motion, being second-order differential equations containing also first-order terms, are in the form of a quadratic eigenvalue problem. The quadratic eigenvalue problem is solved by the formation of a generalized eigenvalue problem. Following the solution of the generalized eigenvalue problem and reduction to natural frequencies and mode shapes, the mode shapes are sorted using the modal assurance criterion (MAC) in order to form the FW and BW divergence pattern of the Campbell diagram.

The objectives of the present work are fourfold:

1. Expound a clear and comprehensive presentation of all the steps of the finite element derivation for the modal analysis of a rotating axisymmetric structure, including gyroscopic effects.

2. Bridge the gap between derivations of varying authorship.
3. Make the method accessible to engineers having an introductory level of understanding in computational methods for structural dynamics.
4. Demonstrate the adequacy of this derivation by comparing results against others published and those of commercial finite element software.

To accomplish these objectives the questions of: how is an axisymmetric element that accounts for variation in the circumferential direction formulated, how is a gyroscopic damping matrix formulated, how is the mathematical derivation of Geradin and Kill [4] linked to the explicit matrix definition of the gyroscopic damping matrix given by Stephenson and Rouch [8], how is a modal analysis performed for differential equations containing first- and second-order terms, and how are the system mode shapes and natural frequencies extracted from the solution of the generalized eigenvalue problem are answered.

In sum, the present work demonstrates that axisymmetric harmonic elements provide accurate computation of natural frequencies and mode shapes and are less computationally demanding than three-dimensional solid elements and that their implementation is available to engineers of advancing expertise in computational methods for structural dynamics.

An overview of the methodologies employed is now given. The elemental mass, gyroscopic damping, and stiffness matrix and the dynamic equations of motion are derived from Hamilton's principle. All element formulations assume the use of cylindrical coordinates, the geometric and material axisymmetry of the structure, and the use of element mapping to isoparametric coordinates.

The second chapter of this work will review the literature of finite element formulations for rotating machinery, including gyroscopic effects. The third chapter will introduce two model shafts that will be utilized in the sample analyses to validate the adequacy of the derivations

presented. The fourth chapter derives the mass, gyroscopic damping, and stiffness matrices as well as the dynamic equations of motion for the axisymmetric harmonic finite element. It also presents an appropriate solution method and offers a procedure for producing a Campbell diagram. The fifth chapter presents the results of four sample analyses performed using the two model shafts and compares the results of the implementation of the presented derivations against other published results and those of commercial finite element software. The sixth chapter lists the limitations of the present work. The seventh chapter draws conclusions on the findings of this work. The eighth and final chapter proposes several directions for future work.

2 LITERATURE REVIEW

Nelson and McVaugh [3] presented mass, gyroscopic damping, and stiffness matrices for an axially rotating beam element. Matrices for rigid disks modeled as lumped masses were also developed.

Geradin and Kill [4] derived an axisymmetric harmonic element, including gyroscopic effects, from first principles. Displacements were defined using a Fourier series expansion in the circumferential direction. Equations for element matrices were discretized for the harmonic having one nodal wave which yields lateral bend modes. Matrix reduction was employed, and the solution of the quadratic eigenvalue problem by transformation to a generalized eigenvalue problem was demonstrated. The formulation was shown to be adequate by use of a sample analysis. The work did not give elements matrices explicitly, however.

Vance *et al.* [5] performed a study of the accuracy of turbomachinery critical speed and mode shape prediction calculated using computer programs. Transfer matrix elements were used in their analysis of three model shafts—a short shaft, a long shaft, and a three-disk laboratory rotor.

Arora [6] developed a cubic axisymmetric harmonic elements from first principles. The mass, gyroscopic damping, and stiffness matrices were derived; however, the gyroscopic damping matrix formulation was shown to be incorrect. Results were presented and compared to those of Vance *et al.* [5] for the three model shafts.

Stephenson, Rouch, and Arora [7] presented results of a cubic axisymmetric harmonic element used in the modal analysis of the three-disk laboratory rotor. Results were compared to those of Vance *et al.* [5], beam finite elements with consistent mass matrices, and axisymmetric

solid elements of commercial finite element software. Only mass and stiffness matrices were used in the cubic axisymmetric harmonic elements.

Stephenson and Rouch [8] gave the gyroscopic damping matrix derived in Geradin and Kill [4] explicitly. The dynamic equations of motion coupling the symmetric and antisymmetric degrees of freedom were shown. Matrix reduction was performed and the formulation was shown to be adequate in several sample analyses, including that of the three-disk rotor. Though the gyroscopic damping matrix was explicitly reported, the steps of derivation from Geradin and Kill [4] to its final formulation were not given.

Cook [9] presents a thorough axisymmetric harmonic element derivation defining displacements in cylindrical coordinates using a Fourier series expansion in the circumferential direction. The formulation reports the relevant element matrices, including the shape function, strain-displacement, and stress-strain matrices. The presentation focused on those terms which are symmetric with respect to the circumferential coordinate and did not present their axisymmetric counterparts. The derivation of a gyroscopic damping matrix was not attempted.

3 DESCRIPTION OF MODELS

Two model shafts, which will be used in the sample analyses, are described. For each model shaft, its geometric and material properties are given. A three-dimensional rendering, as well as a half-meridional cross-section (both to scale), are displayed. These models were selected based on their prior development and analysis in Vance *et al.* [5] and Arora [6] to verify the adequacy of finite element software implementations. The model shafts are used in the Results chapter to demonstrate the adequacy of the implementation of the present finite element derivation. The analysis of the model shafts will include the calculation of natural frequencies and mode shapes.

3.1 Long Shaft (Model Shaft 1)

The first model to be used during the sample analyses is a free-free long steel shaft with the geometric dimensions and material properties listed below. The long shaft is displayed in Figure 3.1.

r_o = 0.038 m	ρ = 7.83 x 10^3 kg/m^3
L = 1.28 m	E = 2.07 x 10^{11} N/m^2
	ν = 0.3

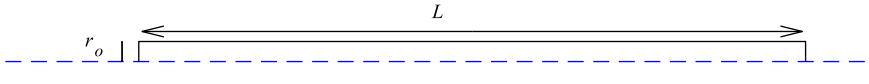

Figure 3.1: Half-meridional cross-section of long shaft

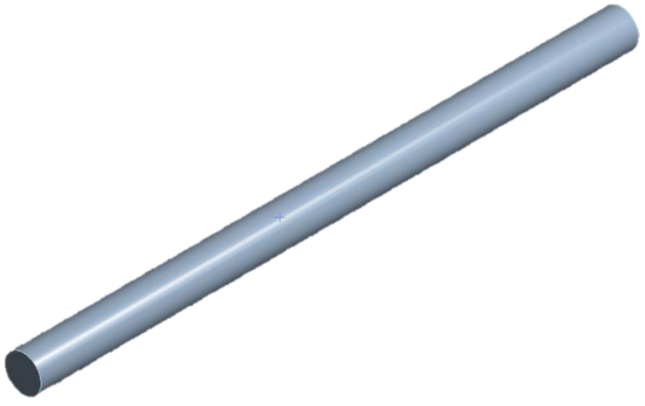

Figure 3.2: Three-dimensional view of long shaft

The percent errors of the natural frequencies of the long shaft will be compared against those published in Vance *et al.* [5] and Arora [6] as well as against those produced by commercial finite element software. The mode shapes of the long shaft for the first several modes will be compared against the results presented in Vance *et al.* [5].

3.2 Long Shaft with Disk (Model Shaft 2)

The model properties are the same as those of model shaft 1 with the following additions.

$r_{disk,o}$ = 0.1152 m
L_{disk} = 0.1278 m
L_{end} = 0.5751 m

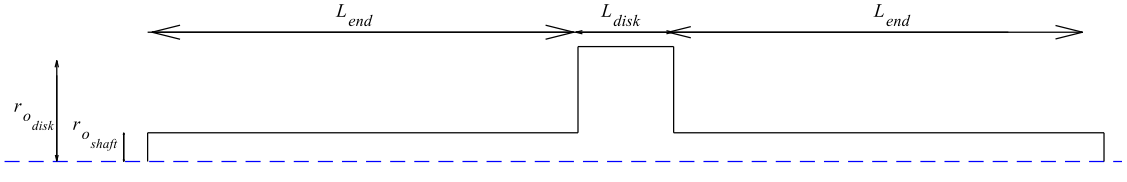

Figure 3.3: Half-meridional cross-section of long shaft

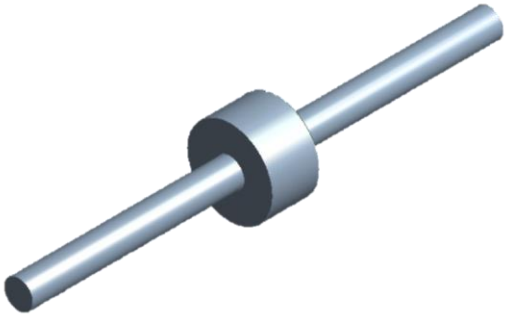

Figure 3.4: Three-dimensional view of long shaft with disk

4 METHODS

The axisymmetric harmonic element matrices and equations of motion are derived using Hamilton's principle, and the matrices are expressed in axisymmetric as well as isoperimetric coordinates. The element matrices are adapted to allow for harmonic variation of displacement with respect to the circumferential coordinate. A solution method for dynamic equations of motion, including gyroscopic effects, is presented, and the use of the modal assurance criterion for mode sorting on Campbell diagrams is discussed.

4.1 Element Selection

The goal of the project is to approximate the three-dimensional deformation of a shaft undergoing relatively high-speed rotations. It is expected the shaft will deform locally, as well as globally (*e.g.*, a whipping motion of the shaft). These deformations are assumed to be governed by linear elasticity theory, where deformations will be assessed in three cylindrical directions: $u(r,\theta,z)$, $v(r,\theta,z)$, $w(r,\theta,z)$. A finite element formulation is used to approximate the solution to the elasticity equations in three-dimensions. Various approaches to spatially discretizing the system are available, including:

- A 3D element model: The model of the shaft could be approximated as a 3D structure using tetrahedral or brick elements. While this approach would provide the greatest modeling flexibility, it would be relatively computationally expensive.
- A beam element model: The shaft could be approximated using line elements to simulate the shaft. This would be relatively computationally inexpensive but would make

simulating the effect of objects on the shaft, such as flywheels or couplers, relatively difficult.

- A standard axisymmetric 2D model: The axisymmetric option would seem to be the best compromise between the 3D and line element model, in terms of computational efficiency and modeling flexibility. However, a standard axisymmetric model cannot simulate the shaft-whip that is known to occur, since all displacements must be independent of the θ coordinate.

To rectify this deficiency, the harmonic axisymmetric element is selected for the current study. Much like the standard axisymmetric element, the body being modeled must be axisymmetric, such that only a planar slice of the cross-section is required for modeling. However, the loading, boundary conditions, and computed results of the harmonic axisymmetric model may vary in the θ direction, providing the ability to model a more general 3D case using planar elements.

A representation of the element is shown below, where the element thickness in the θ direction is modeled as infinitely thin (*i.e.*, modeled on the *r*-*z* plane), but represents a ring of material with differential volume $dV = 2\pi r\, dr\, dz$ where r is the radial distance from the axis of revolution to the centroid of the element, dr is the width of the element in the radial diraction, and dz is the height of the element in the axial direction.

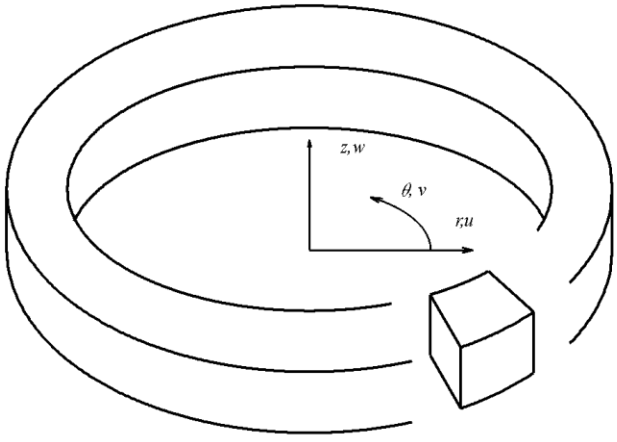

Figure 4.1: Cylindrical coordinate system and axisymmetric element

The deformation field in the *r*-*z* plane of the element is assumed to be approximated using low-order polynomial functions (*i.e.*, linear or quadratic shape functions), as is the norm for a finite element formulation. It is the deformation in the θ direction that is of interest:

- For a 3D element, deformation in the θ direction would also be approximated using a low-order polynomial shape function, thus, requiring meshing in the θ direction.
- For a standard axisymmetric element, deformation in the θ direction is assumed negligible; thus, this term is dropped from the elasticity equations when deriving the FE matrices.
- For the harmonic axisymmetric element, it is assumed that deformation in the θ direction can be approximated using a Fourier series approximation. Thus, rather than using numerous elements with local shape functions to approximate the total θ displacement field, the displacements are approximated using a small number of basis functions which span the entire θ domain (*i.e.*,$0 \leq \theta < 2\pi$) (see Figure 4.2).

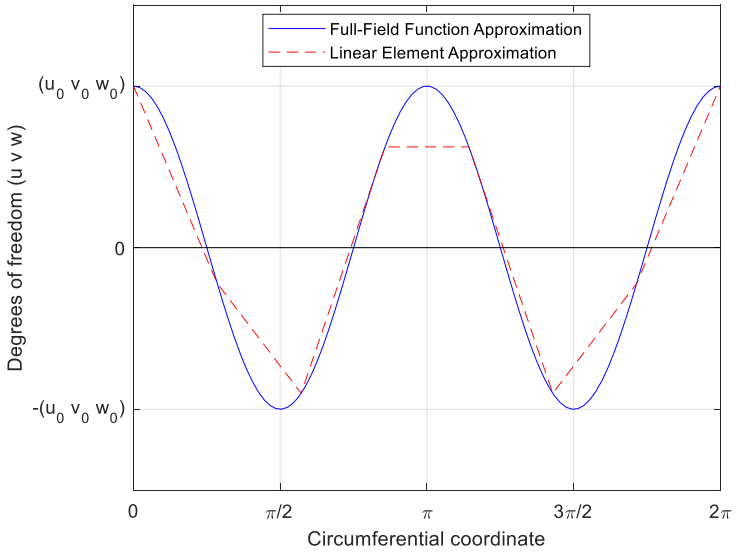

Figure 4.2: Comparison of full-field function and linear element approximations

The resulting approximation of the displacement field variables for the harmonic axisymmetric model are as follows:

$$u(r,\theta,z) = \sum_{n=0}^{\infty} \bar{u}_n(r,z)\cos n\theta + \sum_{n=1}^{\infty} \bar{\bar{u}}_n(r,z)\sin n\theta \qquad 4.1.1a$$

$$v(r,\theta,z) = \sum_{n=1}^{\infty} \bar{v}_n(r,z)\sin n\theta - \sum_{n=0}^{\infty} \bar{\bar{v}}_n(r,z)\cos n\theta \qquad 4.1.1b$$

$$w(r,\theta,z) = \sum_{n=0}^{\infty} \bar{w}_n(r,z)\cos n\theta + \sum_{n=1}^{\infty} \bar{\bar{w}}_n(r,z)\sin n\theta \qquad 4.1.1c$$

where *n* represents the nodal wave number, and $\bar{u}_n(r,z)$, $\bar{\bar{u}}_n(r,z)$, $\bar{v}_n(r,z)$, $\bar{\bar{v}}_n(r,z)$, $\bar{w}_n(r,z)$, and $\bar{\bar{w}}_n(r,z)$ are functions that will be approximated by discretizing the *r*-*z* plane using 2D elements, as is discussed below. The single overbar represents a displacement field that is symmetric about $\theta = 0$ in the *r*- θ plane, while a double overbar represents a displacement field that is antisymmetric about that axis as depicted in Section 1.1. The apparent change in the Fourier series discretization of $v(r,\theta,z)$ is to maintain this grouping of symmetric and antisymmetric displacement fields associated with each of the Fourier terms, purely for the

convenience of interpreting the results; this notational change does not impact the accuracy of the approximation. The reader should note that all terms in Eq. 4.1.1 associated with the sine function do not include the $n = 0$ term (*i.e.*, they are summed for $n = 1,2, ...$). Since $sin(n\theta)$ is equivalent to zero for all θ when $n = 0$, these terms would have no impact on the summation and are thus omitted. This is a necessary step, as one would find in Section 4.5 that the stiffness matrix terms associated with the $sin(n\theta)$ function at $n = 0$ are zero, resulting in a singular stiffness matrix [9]. Additionally, for $n = 0$, the axial translation must be suppressed on at least one node to prevent axial translation [9].

Consider the displacements for a specific nodal wave number (n):

$$\{u_n\} = \{\bar{u}_n\} + \{\bar{\bar{u}}_n\} = \begin{Bmatrix} \bar{u}_n \cos n\theta \\ \bar{v}_n \sin n\theta \\ \bar{w}_n \cos n\theta \end{Bmatrix} + \begin{Bmatrix} \bar{\bar{u}}_n \sin n\theta \\ -\bar{\bar{v}}_n \cos n\theta \\ \bar{\bar{w}}_n \sin n\theta \end{Bmatrix} \tag{4.1.2}$$

It is assumed the symmetric and antisymmetric displacement fields (*i.e.*, $\bar{u}_n(r,z)$, $\bar{\bar{u}}_n(r,z)$, $\bar{v}_n(r,z)$, $\bar{\bar{v}}_n(r,z)$, $\bar{w}_n(r,z)$, and $\bar{\bar{w}}_n(r,z)$) can be approximated using harmonic shape functions, as:

$$\{\bar{u}_n\} = [\bar{N}_n]\{\bar{d}_n\} \tag{4.1.3a}$$

$$\{\bar{\bar{u}}_n\} = [\bar{\bar{N}}_n]\{\bar{\bar{d}}_n\} \tag{4.1.3b}$$

where the symmetric and antisymmetric shape function matrices are:

$$[\bar{N}_n] = \begin{bmatrix} N_1 \cos(n\theta) & 0 & 0 & N_2 \cos(n\theta) & \dots & 0 \\ 0 & N_1 \sin(n\theta) & 0 & 0 & \dots & 0 \\ 0 & 0 & N_1 \cos(n\theta) & 0 & \dots & N_N \cos(n\theta) \end{bmatrix} \tag{4.1.4a}$$

$$[\bar{\bar{N}}_n] = \begin{bmatrix} N_1 \sin(n\theta) & 0 & 0 & N_2 \sin(n\theta) & \dots & 0 \\ 0 & -N_1 \cos(n\theta) & 0 & 0 & \dots & 0 \\ 0 & 0 & N_1 \sin(n\theta) & 0 & \dots & N_N \sin(n\theta) \end{bmatrix} \tag{4.1.4b}$$

Note that these harmonic shape functions utilize standard planar shape functions, $N_1, N_2, \dots, N_N$, which are reviewed in Section 4.2. The symmetric and antisymmetric displacement vectors are defined as:

$$\{\bar{d}_n\} = \{\bar{u}_{1n} \quad \bar{v}_{1n} \quad \bar{w}_{1n} \quad \bar{u}_{2n} \quad \bar{v}_{2n} \quad \bar{w}_{2n} \quad \cdots \quad \bar{w}_{Nn}\} \tag{4.1.5a}$$

$$\{\bar{\bar{d}}_n\} = \{\bar{\bar{u}}_{1n} \quad \bar{\bar{v}}_{1n} \quad \bar{\bar{w}}_{1n} \quad \bar{\bar{u}}_{2n} \quad \bar{\bar{v}}_{2n} \quad \bar{\bar{w}}_{2n} \quad \cdots \quad \bar{\bar{w}}_{Nn}\} \tag{4.1.5b}$$

The displacement fields defined in Equation 4.1.1 can be written in terms of symmetric and antisymmetric nodal displacements as:

$$\{u\} = \sum_{n=0}^{\infty} [\bar{N}_n]\{\bar{d}_n\} + \sum_{n=0}^{\infty} [\bar{\bar{N}}_n]\{\bar{\bar{d}}_n\} \tag{4.1.6}$$

In a standard Fourier series approximation, a relatively large number of *n* terms must be included to converge to an accurate approximation of the function it approximates. In this rotordynamic study, only lateral critical speeds are of interest. Therefore, it is assumed that the rotor is subject to bending deformation only. Since the nodal wave number of $n = 1$ yields the lateral bending modes, the derivation will be done using the symmetric and antisymmetric terms of $n = 1$ only [4, 7, 8]. The breathing and twisting modes of the rotor, modeled by nodal wave number of $n = 0$, will not be computed. While the twisting modes of the shaft will not contribute to rotor blade interference with the casing (*i.e.*, catastrophic failure), they are of paramount importance when designing the rotor from a fatigue failure standpoint. While larger terms of *n* may be included, these would represent local "pinching/bulging" of the shaft (see Figure 1.4). The displacement fields can be approximated as

$$\{u\} = [\bar{N}_1]\{\bar{d}_1\} + [\bar{\bar{N}}_1]\{\bar{\bar{d}}_1\} \tag{4.1.7}$$

This makes the harmonic axisymmetric approximation for the current model a computationally efficient choice: the 3D displacement field dependence on the θ direction is being captured by two full-field Fourier functions, rather than requiring a standard FE mesh in the θ direction as would be required in a 3D model approach.

4.2 Review of Planar, Quadrilateral Isoparametric Elements

As detailed in the previous section, the harmonic axisymmetric element *r*-*z* plane is mapped to the isoparametric element *s*-*t* plane [9]. Figure 4.3 displays this in schematic form.

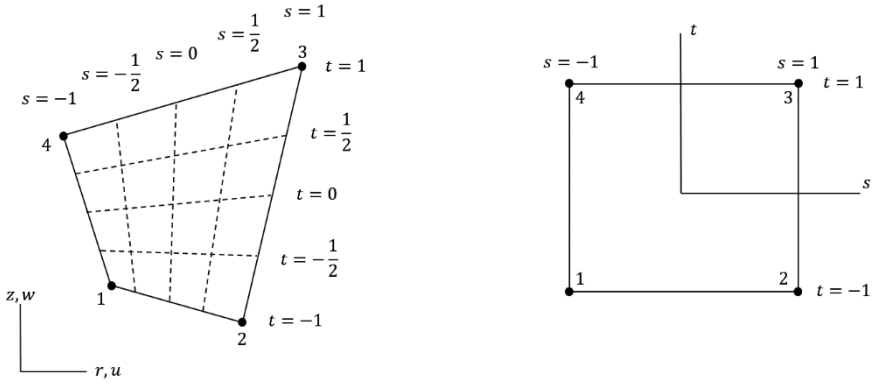

Figure 4.3: Element mapping from cylindrical to isoparametric coordinates [9]

The displacement of any point (r, θ, z) may be interpolated from the nodal displacement. Again, these are functions of the standard planar, quadrilateral shape functions, $N_1, N_2, \dots, N_N$, where N represents the number of nodes per element: 4 for linear elements and 8 for quadratic serendipity elements. These shape functions and the derivatives of the shape functions with respect to s and t are given in Appendix B.

It will be shown that the spatial derivatives of the displacement fields, in terms of (r, θ, z), are necessary to compute the governing equation of motion for the system. Since the shape functions are defined in terms of the local coordinates *s* and *t*, one must be careful when transforming between local and global coordinates. Consider the partial derivative of an arbitrary function $\phi = \phi(r, z)$ with respect to *s* and *t*.

$$\frac{\partial \phi}{\partial s} = \frac{\partial \phi}{\partial r}\frac{\partial r}{\partial s} + \frac{\partial \phi}{\partial z}\frac{\partial z}{\partial s} \qquad \frac{\partial \phi}{\partial t} = \frac{\partial \phi}{\partial r}\frac{\partial r}{\partial t} + \frac{\partial \phi}{\partial z}\frac{\partial z}{\partial t} \qquad 4.2.1$$

This can be written in matrix form as:

$$\begin{Bmatrix} \frac{\partial \phi}{\partial s} \\ \frac{\partial \phi}{\partial t} \end{Bmatrix} = [J] \begin{Bmatrix} \frac{\partial \phi}{\partial r} \\ \frac{\partial \phi}{\partial z} \end{Bmatrix} \quad 4.2.2$$

where the Jacobian matrix is:

$$[J] = \begin{bmatrix} \frac{\partial r}{\partial s} & \frac{\partial z}{\partial s} \\ \frac{\partial r}{\partial t} & \frac{\partial z}{\partial t} \end{bmatrix} = \begin{bmatrix} \sum \frac{\partial N_i}{\partial s} r_i & \sum \frac{\partial N_i}{\partial s} z_i \\ \sum \frac{\partial N_i}{\partial t} r_i & \sum \frac{\partial N_i}{\partial t} z_i \end{bmatrix} = \begin{bmatrix} J_{11} & J_{12} \\ J_{21} & J_{22} \end{bmatrix} \quad 4.2.3$$

for $i = 1,2, \dots, N$. The inverse of the Jacobian matrix may be used if the partial derivatives are in terms of *r* and *z*, while the function (*e.g.*, a shape function) is in terms of *s* and *t*

$$\begin{Bmatrix} \frac{\partial N_i}{\partial r} \\ \frac{\partial N_i}{\partial z} \end{Bmatrix} = [J]^{-1} \begin{Bmatrix} \frac{\partial N_i}{\partial s} \\ \frac{\partial N_i}{\partial t} \end{Bmatrix} \quad 4.2.4$$

The inverse of the Jacobian matrix is:

$$[J]^{-1} = \frac{1}{|J|} \begin{bmatrix} J_{22} & -J_{12} \\ -J_{21} & J_{11} \end{bmatrix} \quad 4.2.5$$

The determinant of the Jacobian matrix is:

$$|J| = \det(J) = J_{1,1} J_{2,2} - J_{2,1} J_{1,2} \quad 4.2.6$$

4.3 Coordinate Systems

Both the Cartesian (x, y, z) and cylindrical *r* (radial), θ (circumferential), and *z* (axial) coordinate systems are used. The relationship between these two coordinate systems is shown in Figure 4.4.

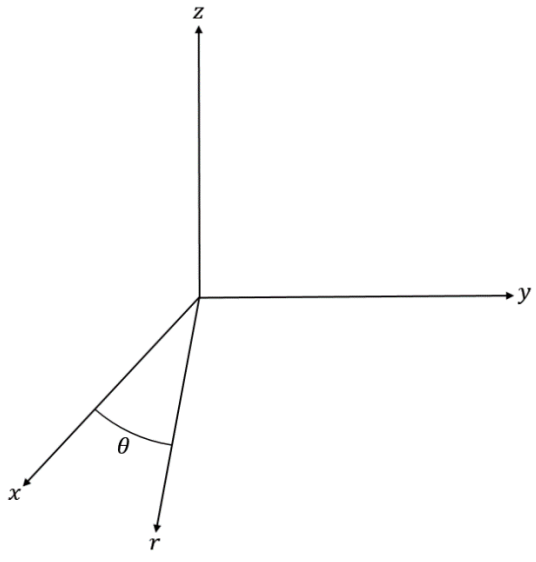

Figure 4.4: Cartesian and cylindrical coordinate systems

The material coordinates of a point within the element in the Cartesian and cylindrical coordinate systems, respectively, are indicated by:

$$\{c\} = \{x \quad y \quad z\}^T \tag{4.3.1a}$$

$$\{c\} = \{r \quad \theta \quad z\}^T \tag{4.3.1b}$$

The displacement at a point within the element in the Cartesian and cylindrical coordinate systems, respectively, are indicated by:

$$\{u_x\} = \{u_x \quad u_y \quad u_z\}^T \tag{4.3.2a}$$

$$\{u\} = \{u \quad v \quad w\}^T \tag{4.3.2b}$$

where variables u_x, u_y, and u_z denote displacements in the Cartesian coordinates *x*, *y*, and *z*, respectively, while u, v, and w denote displacements in the cylindrical coordinates r, θ, and z, respectively.

4.4 Derivation of the Governing Equation of Motion for an Axially Rotating Rotor Using Hamilton's Principle

Various approaches are available for deriving the governing equation of motion for the axially rotating rotor, including Newtonian mechanics, variational methods, and integral methods [11]. Since the kinetic and strain energies of the system are relatively straight-forward to compute in this case, the variational energy approach has been selected.

Hamilton's principle states that the energy functional one wishes to minimize using the variational energy approach [11] is equivalent to

$$L = U - T \tag{4.4.1}$$

where L is referred to as the Lagrangian, U is the potential energy stored in the system, and T is the kinetic energy of the system. This form of Hamilton's principle requires that no nonconservative forces act on the system. This constraint is valid for this investigation since it is assumed that there are no loads acting on the system and the rotor has "free-free" end conditions (*i.e.,* not on bearings). Under these conditions, the variational energy approach can be shown to reduce to the form of Lagrange's equation [11], which is

$$\frac{d}{dt}\left(\frac{\partial L}{\partial \dot{d}}\right) - \frac{\partial L}{\partial d} = 0 \tag{4.4.3}$$

where d represent the displacements of the system (*i.e., u, v, w*), and $\dot{d}$ represent the time derivatives of the displacements (*i.e.,* the velocities).

Kinetic Energy:

Computing the total kinetic energy for the rotor system is no simple task. Since the rotor is an elastodynamic system, the material velocity associated with both global (*i.e.,* rigid-body) and local (*i.e.,* material deformation) motion must be included. The paper by Geradin and Kill [4] involves many pages of derivations to properly account for kinetic energy associated with translational and gyroscopic motion. Rather than replicate this derivation herein, the reader is

invited to consult the original derivation. Instead, the final form of the total kinetic energy is included below as

$$T = T_t + T_g = \frac{1}{2}\int (\dot{u}^2 + \dot{v}^2 + \dot{w}^2)\, dm + \Omega \int \frac{\partial \dot{v}}{\partial z} w\, r\, dm \qquad 4.4.4$$

where $\dot{u}$, $\dot{v}$, and $\dot{w}$ represent the time derivatives of the deformation in the *r*, θ, and *z*, directions, respectively, Ω is the spin-rate of the rotor, and $\int dm$ represents a mass integral over the entire system.

Consider the translational kinetic energy term, T_t, in Equation 4.4.4. The velocity at a point (*s*,*t*) within the element is calculated by taking the time derivative of Equation 4.1.7:

$$\{\dot{u}\} = [\bar{N}_1]\left\{\dot{\bar{d}}_1\right\} + [\bar{\bar{N}}_1]\left\{\dot{\bar{\bar{d}}}_1\right\} \qquad 4.4.5$$

thus,

$$\dot{u}^2 + \dot{v}^2 + \dot{w}^2 = \left\{\dot{\bar{d}}_1\right\}^T [\bar{N}_1]^T [\bar{N}_1]\left\{\dot{\bar{d}}_1\right\} + \left\{\dot{\bar{\bar{d}}}_1\right\}^T [\bar{\bar{N}}_1]^T [\bar{\bar{N}}_1]\left\{\dot{\bar{\bar{d}}}_1\right\} \qquad 4.4.6$$

Incorporating this into the translational kinetic energy term in Equation 4.4.4 yields:

$$T_t = \frac{1}{2}\int \left(\left\{\dot{\bar{d}}_1\right\}^T [\bar{N}_1]^T [\bar{N}_1]\left\{\dot{\bar{d}}_1\right\} + \left\{\dot{\bar{\bar{d}}}_1\right\}^T [\bar{\bar{N}}_1]^T [\bar{\bar{N}}_1]\left\{\dot{\bar{\bar{d}}}_1\right\}\right) \rho dV \qquad 4.4.7$$

or simply

$$T_t = \frac{1}{2}\left\{\dot{\bar{d}}_1\right\}^T [\bar{m}_{e_1}]\left\{\dot{\bar{d}}_1\right\} + \frac{1}{2}\left\{\dot{\bar{\bar{d}}}_1\right\}^T [\bar{\bar{m}}_{e_1}]\left\{\dot{\bar{\bar{d}}}_1\right\} \qquad 4.4.8$$

where

$$[\bar{m}_{e_1}] = \int [\bar{N}_1]^T [\bar{N}_1]\, \rho dV \qquad 4.4.9a$$

$$[\bar{\bar{m}}_{e_1}] = \int [\bar{\bar{N}}_1]^T [\bar{\bar{N}}_1]\, \rho dV \qquad 4.4.9b$$

As shown in Appendix C, since all non-zero indices of the elemental mass matrices contain either $cos^2\theta$ or $sin^2\theta$ and due to the fact that $\int_0^{2\pi} cos^2\theta = \int_0^{2\pi} sin^2\theta = \pi$, the symmetric and antisymmetric mass matrices simplify to:

$$[\bar{m}_e] = [\bar{\bar{m}}_e] = [m_e] = \rho\pi \int_{-b}^{b}\int_{-a}^{a} [N]^T[N] r\, dr dz = \rho\pi \int_{-b}^{b}\int_{-a}^{a} [m] r\, dr dz \tag{4.4.10}$$

The derivation of the gyroscopic kinetic energy is more involved; thus, it has been included in Appendix D. The final form of T_g is:

$$T_g = \{\dot{d}\}^T [c_{e_1}]\{d\} = \left\{\dot{\bar{d}}_1\right\}^T [\bar{c}_{e_1}]\{\bar{d}_1\} + \left\{\dot{\bar{\bar{d}}}_1\right\}^T [\bar{\bar{c}}_{e_1}]\{\bar{\bar{d}}_1\} \tag{4.4.11}$$

Strain Energy:

The strain energy of the flexible rotor is [9]:

$$U = \frac{1}{2}\int \{\sigma\}^T\{\varepsilon\}\, dV \tag{4.4.12}$$

The stress-strain relationship is given by [9]:

$$\{\sigma\} = [E]\{\varepsilon\} \tag{4.4.13}$$

The stress-strain matrix $[E]$ for a linear elastic material in three dimensions using axisymmetric coordinates is:

$$E = \begin{bmatrix} (1-\upsilon)\,c & \upsilon\, c & \upsilon\, c & 0 & 0 & 0 \\ \upsilon\, c & (1-\upsilon)\,c & \upsilon\, c & 0 & 0 & 0 \\ \upsilon\, c & \upsilon\, c & (1-\upsilon)\,c & 0 & 0 & 0 \\ 0 & 0 & 0 & G & 0 & 0 \\ 0 & 0 & 0 & 0 & G & 0 \\ 0 & 0 & 0 & 0 & 0 & G \end{bmatrix} \tag{4.4.14a}$$

$$c = \frac{E}{(1+\upsilon)(1-2\upsilon)} \tag{4.4.14b}$$

The stress, strain, and initial stress vector are defined as:

$$\{\sigma\} = \{\sigma_r \quad \sigma_\theta \quad \sigma_z \quad \tau_{zr} \quad \tau_{r\theta} \quad \tau_{\theta z}\}^T \tag{4.4.15a}$$

$$\{\varepsilon\} = \{\varepsilon_r \quad \varepsilon_\theta \quad \varepsilon_z \quad \gamma_{zr} \quad \gamma_{r\theta} \quad \gamma_{\theta z}\}^T \tag{4.4.15b}$$

For an isotropic material, the strains are defined as:

$$\varepsilon_r = \frac{\partial u}{dr} \qquad \varepsilon_\theta = \frac{u}{r} + \frac{\frac{\partial v}{d\theta}}{r} \qquad \varepsilon_z = \frac{\partial w}{dz}$$

$$\gamma_{zr} = \frac{\partial u}{dz} + \frac{\partial w}{dr} \qquad \gamma_{r\theta} = \frac{\frac{\partial u}{d\theta}}{r} + \frac{\partial v}{dr} - \frac{v}{r} \qquad \gamma_{\theta z} = \frac{\partial v}{dz} + \frac{\frac{\partial w}{d\theta}}{r} \tag{4.4.16}$$

Strains are calculated from the displacements using the operator matrix:

$$\{\varepsilon\} = [\partial]\{u\} \tag{4.4.17}$$

where the displacement vector is defined in Equation 4.1.7 and the differential operator is defined as:

$$[\partial] = \begin{bmatrix} \partial/\partial r & 0 & 0 \\ 1/r & (\partial/\partial\theta)/r & 0 \\ 0 & 0 & \partial/\partial z \\ \partial/\partial z & 0 & \partial/\partial r \\ (\partial/\partial\theta)/r & \partial/\partial r - 1/r & 0 \\ 0 & \partial/\partial z & (\partial/\partial\theta)/r \end{bmatrix} \tag{4.4.18}$$

The strain-displacement matrix $[B]$ relates the displacement vector to the strain vector:

$$\{\varepsilon\} = [B]\{d\} = [\bar{B}_1]\{\bar{d}_1\} + [\bar{\bar{B}}_1]\{\bar{\bar{d}}_1\} \tag{4.4.19}$$

Thus, according to Equations 4.1.7 and 4.4.17, the strain-displacement matrix is calculated as:

$$[B] = [\partial][N] = [\partial]\{\bar{N}_1\} + [\partial]\{\bar{\bar{N}}_1\} \tag{4.4.20}$$

The strain-displacement matrices for $n = 1$ nodal waves are:

$$[\bar{B}_1] = \begin{bmatrix} \frac{\partial N_1}{\partial r}\cos(1\theta) & 0 & 0 & \frac{\partial N_2}{\partial r}\cos(1\theta) & \cdots & 0 \\ \frac{N_1}{r}\cos(1\theta) & \frac{N_1}{r}\cos(1\theta) & 0 & \frac{N_2}{r}\cos(1\theta) & \cdots & 0 \\ 0 & 0 & \frac{\partial N_1}{\partial z}\cos(1\theta) & 0 & \cdots & \frac{\partial N_N}{\partial z}\cos(1\theta) \\ \frac{\partial N_1}{\partial z}\cos(1\theta) & 0 & \frac{\partial N_1}{\partial r}\cos(1\theta) & \frac{\partial N_2}{\partial z}\cos(1\theta) & \cdots & \frac{\partial N_N}{\partial r}\cos(1\theta) \\ -\frac{N_1}{r}\sin(1\theta) & \left(\frac{\partial N_1}{\partial r} - \frac{N_1}{r}\right)\sin(1\theta) & 0 & -\frac{N_2}{r}\sin(1\theta) & \cdots & 0 \\ 0 & \frac{\partial N_1}{\partial z}\sin(1\theta) & -\frac{N_1}{r}\sin(1\theta) & 0 & \cdots & -\frac{N_N}{r}\sin(1\theta) \end{bmatrix} \tag{4.4.21a}$$

4.4.21b

$$\left[\bar{\bar{B}}_1\right] = \begin{bmatrix} \frac{\partial N_1}{\partial r}\sin(1\theta) & 0 & 0 & \frac{\partial N_2}{\partial r}\sin(1\theta) & \cdots & 0 \\ \frac{N_1}{r}\sin(1\theta) & \frac{N_1}{r}\sin(1\theta) & 0 & \frac{N_2}{r}\sin(1\theta) & \cdots & 0 \\ 0 & 0 & \frac{\partial N_1}{\partial z}\sin(1\theta) & 0 & \cdots & \frac{\partial N_N}{\partial z}\sin(1\theta) \\ \frac{\partial N_1}{\partial z}\sin(1\theta) & 0 & \frac{\partial N_1}{\partial r}\sin(1\theta) & \frac{\partial N_2}{\partial z}\sin(1\theta) & \cdots & \frac{\partial N_N}{\partial r}\sin(1\theta) \\ \frac{N_1}{r}\cos(1\theta) & -\left(\frac{\partial N_1}{\partial r} - \frac{N_1}{r}\right)\cos(1\theta) & 0 & \frac{N_2}{r}\cos(1\theta) & \cdots & 0 \\ 0 & -\frac{\partial N_1}{\partial z}\cos(1\theta) & \frac{N_1}{r}\cos(1\theta) & 0 & \cdots & \frac{N_N}{r}\cos(1\theta) \end{bmatrix}$$

Substituting the equation for stress, the strain energy of the flexible rotor is:

$$U = \frac{1}{2}\int \{\sigma\}^T\{\varepsilon\}\, dV = \frac{1}{2}\int \{\varepsilon\}^T[E]\{\varepsilon\}\, dV \qquad 4.4.22$$

Making the substitution $\{\varepsilon\} = [B]\{d\}$ yields:

$$\begin{aligned} U &= \frac{1}{2}\int \{d\}^T[B]^T[E][B]\{d\}\, dV \\ &= \frac{1}{2}\int \left(\{\bar{d}_1\}^T[\bar{B}_1]^T[E][\bar{B}_1]\{\bar{d}_1\} + \{\bar{\bar{d}}_1\}^T\left[\bar{\bar{B}}_1\right]^T[E]\left[\bar{\bar{B}}_1\right]\{\bar{\bar{d}}_1\}\right) dV \end{aligned} \qquad 4.4.23$$

which simplifies to:

$$U = \frac{1}{2}\{d\}^T[k_e]\{d\} = \frac{1}{2}\{\bar{d}_1\}^T[\bar{k}_{e_1}]\{\bar{d}_1\} + \frac{1}{2}\{\bar{\bar{d}}_1\}^T[\bar{\bar{k}}_{e_1}]\{\bar{\bar{d}}_1\} \qquad 4.4.24$$

where:

$$\left[\bar{k}_{e_1}\right] = \int [\bar{B}_1]^T[E][\bar{B}_1]\, dV \qquad 4.4.25a$$

$$\left[\bar{\bar{k}}_{e_1}\right] = \int \left[\bar{\bar{B}}_1\right]^T[E]\left[\bar{\bar{B}}_1\right] dV \qquad 4.4.25b$$

As shown in Appendix C, the symmetric and antisymmetric stiffness matrices simplify to:

$$\left[\bar{k}_e\right] = \left[\bar{\bar{k}}_e\right] = [k_e] = \pi \int_{-b}^{b}\int_{-a}^{a} [B]^T[E][B] r\, dr dz \qquad 4.4.26$$

Dynamic equations of motion:

Now that that the kinetic and potential energies have been formulated, the Lagrangian written in terms of the elemental matrices is:

$$L = \frac{1}{2}\left[\dot{d}\right]^T [m_e]\left[\dot{d}\right] + \left\{\dot{d}\right\}^T [c_e]\{d\} - \frac{1}{2}\{d\}^T [k_e]\{d\} \qquad 4.4.27$$

The derivatives of Equation 4.4.3 are:

$$\frac{\partial L}{\partial \dot{d}} = [m_e]\left[\dot{d}\right] + [c_e]\{d\} + 0 \qquad 4.4.28a$$

$$\frac{\partial}{\partial t}\left(\frac{\partial L}{\partial \dot{d}}\right) = [m_e]\left[\ddot{d}\right] + [c_e]\left\{\dot{d}\right\} \qquad 4.4.28b$$

$$\frac{\partial L}{\partial d} = -[k_e]\{d\} \qquad 4.4.28c$$

Substitution of Equations 4.4.28 into Equation 4.4.3 gives the equations of motion:

$$\frac{d}{dt}\left(\frac{\partial L}{\partial \dot{d}}\right) - \frac{\partial L}{\partial d} = [m_e]\left[\ddot{d}\right] + [c_e]\left\{\dot{d}\right\} + [k_e]\{d\} = 0 \qquad 4.4.29$$

4.5 Elemental Mass, Damping, and Stiffness Matrices Expressed in Axisymmetric and Isoparametric Coordinates

The elemental matrices are now summarized and transformed into isoparametric coordinates.

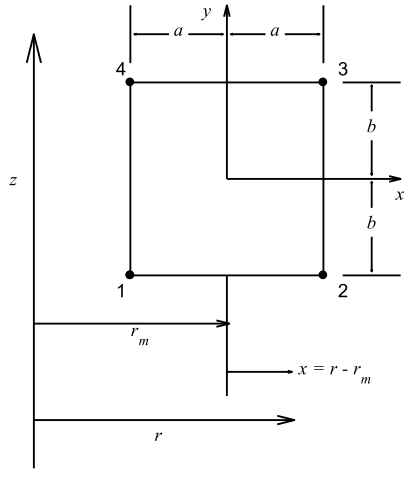

Figure 4.5: Half-meridional cross-section of axisymmetric element [9]

The single- and double-bar elemental mass, gyroscopic damping, and stiffness matrices are written in the axisymmetric coordinates system. Since the gyroscopic damping matrix is independent of θ, it is expressed by only one equation.

$$[c_e] = \pi\Omega\rho \int_{-b}^{b}\int_{-a}^{a} [C] r^2 \, dr dz \tag{4.5.1a}$$

$$[m_e] = \rho\pi \int_{-b}^{b}\int_{-a}^{a} [N]^T [N] r \, dr dz \tag{4.5.1b}$$

$$[k_e] = \pi \int_{-b}^{b}\int_{-a}^{a} [B]^T [E] [B] r \, dr dz \tag{4.5.1c}$$

$$r = r_m + x \tag{4.5.2}$$

Transforming to the isoparametric coordinate system, the elemental mass, gyroscopic damping, and stiffness matrices are written:

$$[c_e] = \pi\Omega\rho \int_{-1}^{1}\int_{-1}^{1} [C] r(s,t)^2 |J| \, ds dt \tag{4.5.3a}$$

$$[m_e] = \rho\pi \int_{-1}^{1}\int_{-1}^{1} [N]^T [N] r(s,t) |J| \, ds dt \tag{4.5.3b}$$

$$[k_e] = \pi \int_{-1}^{1}\int_{-1}^{1} [B]^T [E] [B] r(s,t) |J| \, ds dt \tag{4.5.3c}$$

The elemental gyroscopic damping matrix couples the bending of the shaft in the two orthogonal directions perpendicular to the shaft axis; therefore, a skew-symmetric damping matrix must be formulated for the elemental dynamic equations of motion [8]. The mass and stiffness matrices are symmetric.

$$\begin{bmatrix}[m_e] & [0]\\ [0] & [m_e]\end{bmatrix}\begin{Bmatrix}\{\ddot{\bar{d}}\}\\ \{\ddot{\bar{d}}\}\end{Bmatrix}+\begin{bmatrix}[0] & [c_e]\\ [-c_e] & [0]\end{bmatrix}\begin{Bmatrix}\{\dot{\bar{d}}\}\\ \{\dot{\bar{d}}\}\end{Bmatrix}+\begin{bmatrix}[k_e] & [0]\\ [0] & [k_e]\end{bmatrix}\begin{Bmatrix}\{\bar{d}\}\\ \{\bar{d}\}\end{Bmatrix}=\begin{Bmatrix}\{0\}\\ \{0\}\end{Bmatrix} \quad 4.5.4$$

The elemental equations of motion are written in compact form:

$$[m_e^*]\{\ddot{d}\}+[c_e^*]\{\dot{d}\}+[k_e^*]\{d\}=\{0\} \quad 4.5.5$$

Elemental mass, damping, and stiffness matrices are assembled into global mass, damping, and stiffness matrices using standard procedures, which yields the global dynamic equations of motion.

$$[M]\{\ddot{D}\}+[C]\{\dot{D}\}+[K]\{D\}=\{0\} \quad 4.5.6$$

Rigid-body translations parallel to the $r\theta$ plane and rigid-body rotations about axes in this plane are possible for $n=1$. These will result as rigid body modes, with frequencies of 0 Hz, during the modal analysis unless appropriate constraints are added in the respective directions [9].

4.6 Solution Method for Dynamic Equations of Motion Including Gyroscopic Effects

A method is presented to solve the global dynamic equations of motion, which is in the form of a quadratic eigenvalue problem [4]. Assuming the displacements take the exponential form:

$$D=ve^{pt} \quad 4.6.1a$$

$$\dot{D}=pve^{pt}=pD \quad 4.6.1b$$

$$\ddot{D}=p^2ve^{pt}=p\dot{D} \quad 4.6.1c$$

$$p[I]\{D\}=[I]\{\dot{D}\} \quad 4.6.1d$$

The quadratic eigenvalue problem can be solved by transforming it into a generalized eigenvalue problem.

$$p[M]\{\dot{D}\} + p[C]\{D\} + [K]\{D\} = \{0\} \tag{4.6.2a}$$

$$p\begin{bmatrix}[I] & [0]\\ [C] & [M]\end{bmatrix}\begin{Bmatrix}\{D\}\\ \{\dot{D}\}\end{Bmatrix} + \begin{bmatrix}[0] & [-I]\\ [K] & [0]\end{bmatrix}\begin{Bmatrix}\{D\}\\ \{\dot{D}\}\end{Bmatrix} = \begin{Bmatrix}\{0\}\\ \{0\}\end{Bmatrix} \tag{4.6.2b}$$

The generalized eigenvalue problem is written in compact form:

$$p[A]\{U\} + [B]\{U\} = \{0\} \tag{4.6.3a}$$

$$p[A]\{U\} = -[B]\{U\} \tag{4.6.3b}$$

The solution of the generalized eigenvalue problem yields $\{\Lambda\}$ and $[\Psi]$.

The stabilities $\{s\}$ and natural frequencies $\{\lambda\}$ (eigenvalues) of the system are the real and imaginary parts, respectively, of the second half of the solution vector $\{\Lambda\}$ of eigenvalues.

$$\{\Lambda\} = \begin{Bmatrix}\vdots\\ \{s\} + \{i\lambda\}\end{Bmatrix} \tag{4.6.4}$$

The matrix of mode shape column vectors (eigenvectors) of the system $[\psi]$ is the quadrant of the solution matrix composed of the second half of its rows and columns.

$$[\Psi] = \begin{bmatrix}\ddots & \vdots\\ \dots & [\psi]\end{bmatrix} \tag{4.6.5}$$

Table 1 shows the size of the matrices and vectors used throughout the solution process given that there are three degrees of freedom (r, θ, z) per node, N is the number of nodes per element, and M is the total number of nodes in the model.

Table 1: Size of matrices

Element matrices *before* coupling symmetric and antisymmetric DOF to include gyroscopic effects	$[m_e]$ $[c_e]$ $[k_e]$ *3N* x *3N*
Element matrices *after* coupling symmetric and antisymmetric DOF to include gyroscopic effects	$[m_e^*]$ $[c_e^*]$ $[k_e^*]$ *6N* x *6N*
Global matrices	$[M]$ $[C]$ $[K]$ *6M* x *6M*
Generalized eigenvalue problem matrices	$[A]$ $[B]$ *12M* x *12M*
Solution matrices	$[\Psi]$ $\{\Lambda\}$ *12M* x *12M*
Matrix of eigenvectors and vector of eigenvalues	$[\psi]$ $\{\lambda\}$ *6M* x *6M*

4.7 Use of Modal Assurance Criterion for the Purpose of Mode Sorting on Campbell Diagram

When performing modal analyses at successive speeds, the order in which mode shapes and their associated natural frequencies appear may change from one speed to the next, so it is necessary to sort the modes [10]. An example of this is illustrated in Table 2.

Table 2: Mode shapes appearing in different order

	Operating Speed (rpm)	
Mode	5,000	7,000
1	195 Hz (mode A)	185 Hz (mode B)
2	200 Hz (mode B)	205 Hz (mode A)

At a lower operating speed, the mode shape *B* may occur at a higher natural frequency than mode shape *A*, whereas at a higher operating speed, the mode shape *B* may occur at a lower natural frequency than mode shape *A*. Therefore, the modal assurance criterion (MAC) number is used to ensure each mode shape is appropriately tracked throughout the entire operating speed range used in a Campbell diagram analysis [10]. The MAC number determines the degree of orthogonality between two mode shape vectors produced by modal analysis. A MAC number near 0 indicates the mode shapes are near orthogonal and, therefore, do not belong to the same mode. A MAC number near 1 indicates the modes shapes are almost identical and, therefore, belong to the same mode. The MAC number is defined as:

$$MAC\left(\{u\}_i^k, \{u\}_j^{k+1}\right) = \frac{(\{\bar{u}\}_i^{k\,T} \cdot \{m\} \cdot \{u\}_j^{k+1}) \cdot (\{u\}_i^{k\,T} \cdot \{m\} \cdot \{\bar{u}\}_j^{k+1})}{(\{\bar{u}\}_i^{k\,T} \cdot \{m\} \cdot \{u\}_i^{k}) \cdot (\{\bar{u}\}_j^{k+1\,T} \cdot \{m\} \cdot \{u\}_j^{k+1})} \qquad 4.7.1$$

where the overbar indicates the complex conjugate, the superscripts k and $k+1$ indicate whether the mode was calculated at the k^{th} or $(k+1)^{th}$ operating speeds, the subscripts i and j indicate the i^{th} and j^{th} mode (in the order from lowest to highest natural frequency), and $\{m\}$ is the diagonal of the mass matrix.

For each nodal wave number (n) used in the analysis, the following calculation is performed at each tested operating speed k from the first operating speed to the second to last operating speed: For each mode shape calculated at operating speed k, the MAC number is calculated for each mode shape at operating speed $k+1$; the mode shape at operating speed $k+1$ with MAC number closest to 1 is selected as the next mode shape for that particular mode at the next tested operating speed.

5 RESULTS OF SAMPLE ANALYSES AND VALIDATION AGAINST COMMERCIAL FINITE ELEMENT SOFTWARE RESULTS

This chapter presents and discusses the results generated from four sample analyses using the two model shafts presented in Chapter 3. The first analysis is a modal analysis without rotation performed on model shaft 1 and compares the mode shapes against those produced by commercial finite element software. The second analysis is a modal analysis performed on model shaft 1 rotating at 10,000 rpm. The third analysis compares a Campbell diagram against that produced by commercial finite element software for the long shaft (model shaft 1). The fourth analysis is a modal analysis of a long shaft with disk (model shaft 2) and investigates the differences of omitting the disk geometry and replacing it with a portion of shaft having increased density so that the shaft has the same mass as the shaft with a disk.

For each sample analysis, a mesh convergence was performed by calculating the first four natural frequencies for incremental mesh refinements and comparing the percent errors of natural frequencies yielded by each mesh. The first four modes were checked for convergence because the modes above them had "high" frequencies relative to the range of interest (*i.e.*, above excitable frequencies). Mesh convergence was investigated in the axial as well as in the radial directed. It was found that for the model shafts used having more than one element in the radial direction did not significantly improve the accuracy of natural frequency prediction; thus, only one element in the radial direction was used to ensure the least amount of computational resources necessary were used. The reason for this behavior is most likely due to the relatively "thin" nature of the shafts. The mesh was selected that met one of the criteria below.

1. The mesh yielded the lowest percent errors of natural frequencies on average for the range of the modes of interest *e.g.*, a global minimum on a percent error against the number of nodes plot as shown in Figure 5.1a.

2. The mesh using the least number of nodes where the percent errors of the natural frequencies calculated using that mesh were all below the selected criterion of percent error, as shown by Figure 5.1b. The selected criterion of percent error was chosen to be 3% error in order to approximately match the percent error of the published results.

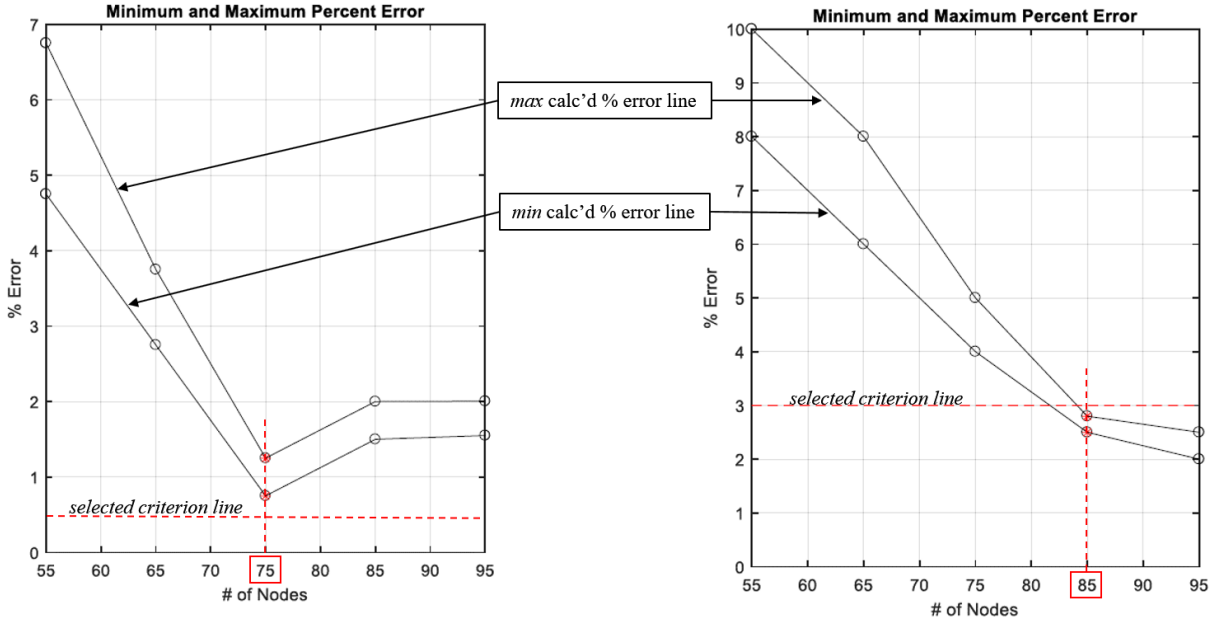

(a) **(b)**

Figure 5.1: (a) mesh convergence criterion 1, (b) mesh convergence criterion 2

5.1 Validation Modal Analysis without Shaft Rotation for Long Shaft Model

A modal analysis was performed for the long shaft (model shaft 1). The mesh was generated using rectangular axisymmetric harmonic elements on a half-meridional cross-section of the shaft. The analysis was performed first using linear elements. The mesh using linear elements is shown in Figure 5.2.

Figure 5.2: Mesh of non-rotating long shaft using linear elements

The analysis was performed again using quadratic elements. The mesh using quadratic elements is shown in Figure 5.3.

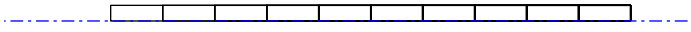

Figure 5.3: Mesh of non-rotating long shaft using quadratic elements

A mesh convergence was performed for the analyses. Figure 5.4 displays the mesh convergence plots.

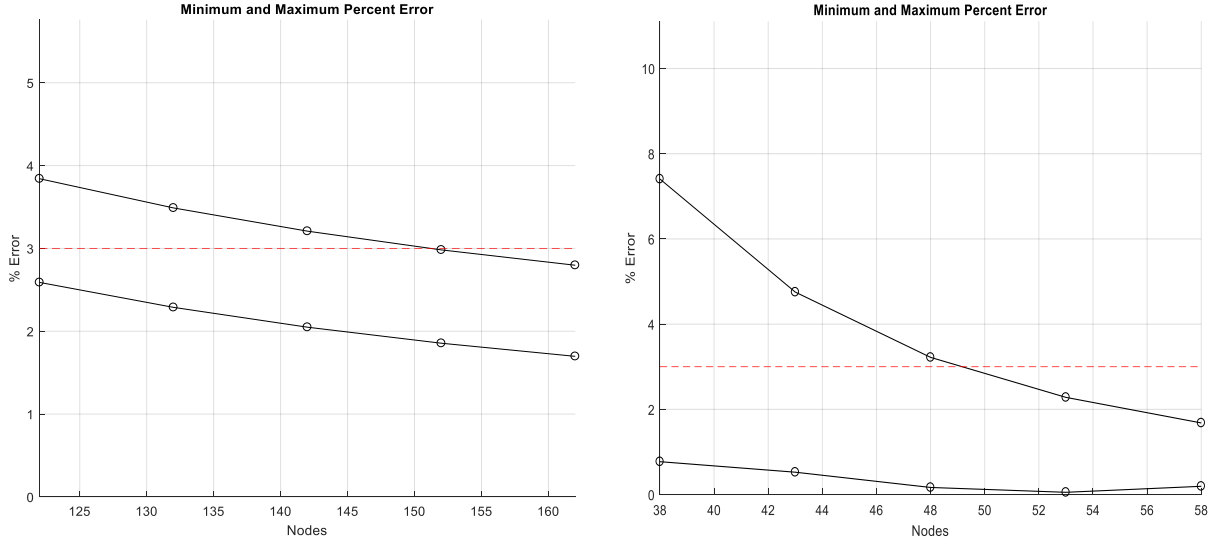

(a) **(b)**

Figure 5.4: Mesh convergence of non-rotating long shaft: (a) linear, (b) quadratic

The linear model converged to the criterion using 152 nodes (456 DOF). The quadratic model converged to the criterion using 53 nodes (159 DOF). The first four computed natural frequencies of the long shaft compared with published results and their associated percent errors against the measured natural frequencies are displayed in Table 3.

Table 3: Comparison of natural frequencies for non-rotating long shaft

		Case 1:		**Case 2:**		**Case 3:**		**Case 4:**		**Case 5:**	
Mode	Measured [5]	ANSYS WB		Linear Model		Quadratic Model		Vance *et al.* [5]		Arora [6]	
1	212.5	210.0	(-1.18)	218.1	(2.65)	213.5	(0.46)	210.9	(-0.75)	211.2	(-0.61)
2	581.2	569.0	(-2.10)	592.0	(1.86)	580.9	(-0.05)	567.4	(-2.37)	568.1	(-2.25)
3	1106.2	1091.0	(-1.37)	1135.8	(2.67)	1119.7	(1.22)	1077.5	(-2.59)	1107.0	(0.07)
4	1775.0	1753.0	(-1.24)	1827.9	(2.98)	1815.5	(2.28)	1714.8	(-3.39)	1766.3	(-0.49)

The diversity of element types is noted: Vance *et al.* [5] uses transfer matrix elements, Arora [6] performs the analysis with cubic axisymmetric harmonic elements, and the Linear and Quadratic Models use linear and quadratic axisymmetric harmonic elements, respectively. For the first natural frequency, the percent error in Cases 3, 4, and 5 are less than 1% whereas the percent error in Case 2 is greater than 2.5%. For the second natural frequency, only Case 3 has a percent error less than 1% showing great adequacy with a percent error of -0.05%; Case 2 has a percent error less than 2% and those of Cases 3 and 4 are less than 2.5%. In the third natural frequency, the cubic axisymmetric harmonic elements of Arora [6] display the greatest accuracy with a percent error of 0.07%. Case 3 has a percent error of less than 1.25% and those of Cases 4 and 2 are less than 2.75%. For the fourth natural frequency, the cubic axisymmetric harmonic elements of Arora [6] again exhibit the greatest accuracy with a percent error of -0.49%. The fourth natural frequency of Cases 2 and 3 are less than 3% and that of Case 4 is less than 3.5%. This comparison shows that the axisymmetric harmonic elements have lower percent errors than the transfer matrix elements. The higher-order (quadratic and cubic) elements have the greatest accuracy. The quadratic axisymmetric harmonic elements had the lowest percent error in the first

two natural frequencies. The cubic axisymmetric harmonic elements had the lowest percent error in the second two natural frequencies.

The mode shapes for the first four modes for one nodal wave (n = 1) are qualitatively compared in Figures 5.5. All mode shapes, being eigenvectors, are relative and can be scaled by any constant multiplier.

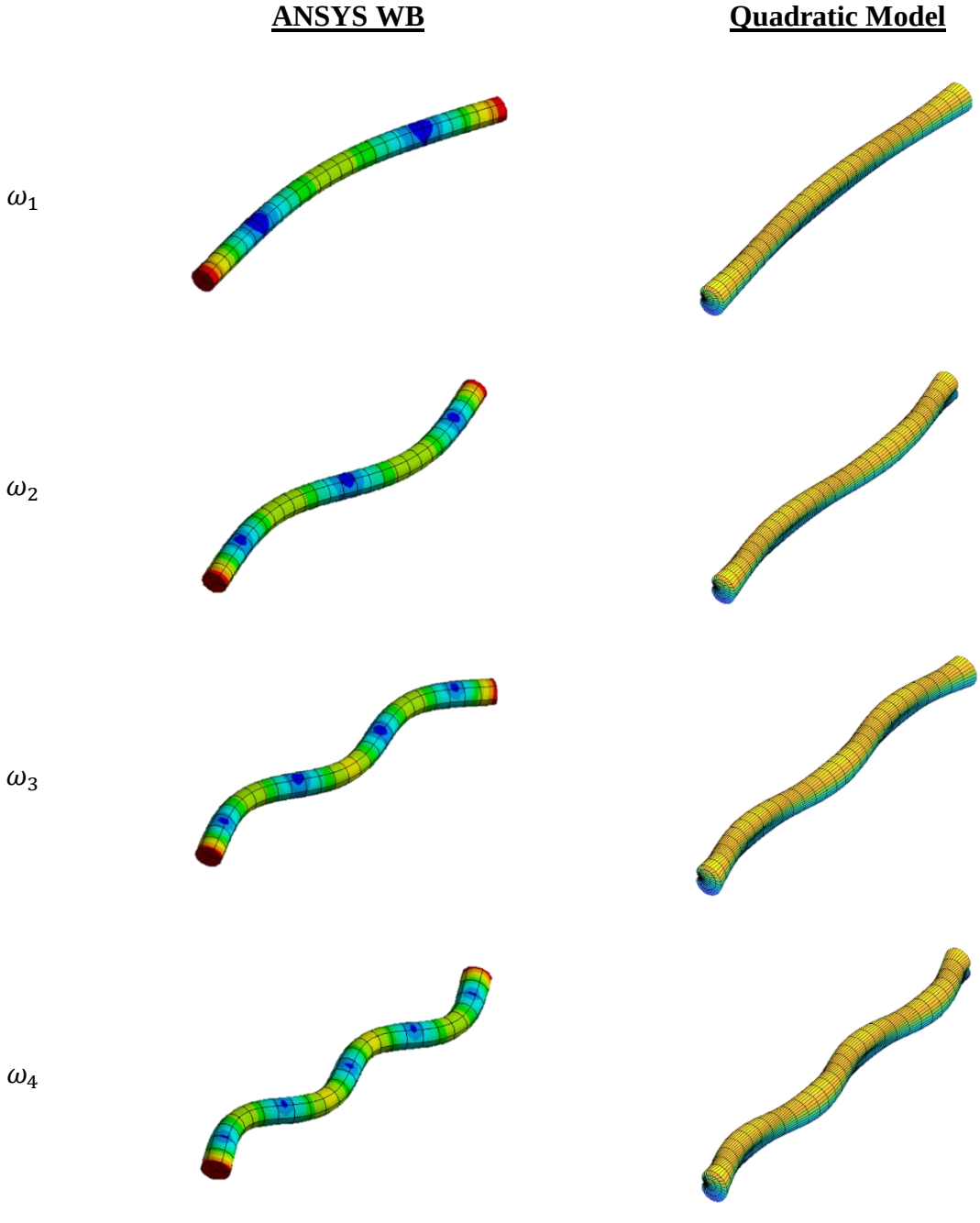

Figure 5.5: Comparison of shaft mode shapes

The bend modes of the shaft (those having one nodal wave) have equal and opposite displacements at θ and $-\theta$. The radial displacement with respect to the axial coordinate of the first bend mode displays the likeness of a half period of a sine wave. Each mode thereafter adds a half period to the sine wave (1, 3/2, *etc*.). It is observed that the cross-section of the mode shapes of the quadratic model appears cardioid rather than circular like the mode shapes of the commercial software. This is attributed to the fact that since cylindrical coordinates are being used, two of which are linear dimensions (r, z) and the third being an angular dimension (θ), a scaling factor would be appropriate to use on the relative deflections in the circumferential direction. The value of such a scaling factor may depend on the geometry of the shaft and is neglected in this study. Insofar as a qualitative comparison is able the mode shapes show good agreement.

5.2 Modal Response of Long Shaft Rotating at 10,000 rpm

A modal analysis was performed for the long shaft (model shaft 1) rotating at 10,000 rpm. The mesh was generated using rectangular axisymmetric harmonic elements on a half-meridional cross-section of the shaft. The analysis was performed first using linear elements. The mesh using linear elements is shown in Figure 5.6.

Figure 5.6: Mesh of rotating long shaft using linear elements

The analysis was performed again using quadratic elements. The mesh using quadratic elements is shown in Figure 5.7.

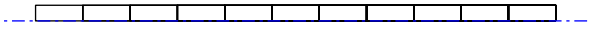

Figure 5.7: Mesh of rotating long shaft using quadratic elements

A mesh convergence was performed for the analyses. Figure 5.8 displays the mesh convergence plots.

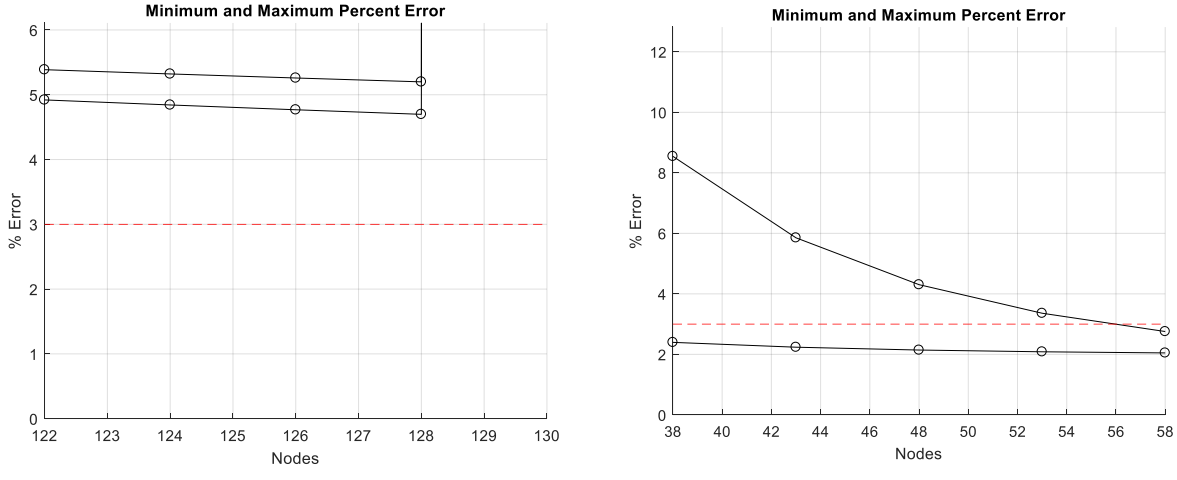

(a) **(b)**

Figure 5.8: Mesh convergence of rotating long shaft: (a) linear, (b) quadratic

The linear model converged to the criterion using 128 nodes (384 DOF). The quadratic model converged to the criterion using 58 nodes (174 DOF). Each bend mode of the shaft diverges into a forward and backward whirl as the operating speed of the shaft increases. This causes the natural frequency of each mode to vary with respect to operating speed. The gyroscopic damping matrix accounts for this phenomenon. The first four forward and backward-whirl natural frequencies of the long shaft and their associated percent errors against those calculated by commercial finite-element software are displayed in Table 4. Since this analysis is performed at an arbitrary operating speed and there are no published results for this model shaft and operating speed, ANSYS Workbench is used as the benchmark.

Table 4: Comparison of natural frequencies for rotating long shaft

Mode	ANSYS WB	Linear Model		Quadratic Model	
1 BW	202	213	(5.45)	207	(2.48)
1 FW	208	218	(4.81)	212	(1.92)
2 BW	551	578	(4.90)	564	(2.36)
2 FW	562	590	(4.98)	575	(2.31)
3 BW	1060	1112	(4.91)	1086	(2.45)
3 FW	1079	1131	(4.82)	1105	(2.41)
4 BW	1711	1792	(4.73)	1758	(2.75)
4 FW	1738	1820	(4.72)	1786	(2.76)

The linear model matches ANSYS Workbench within approximately 5% for all the natural frequencies. The quadratic model matches the ANSYS Workbench model within approximately 2%-2.75% for all the natural frequencies. Both models show accurate natural frequency prediction compared to ANSYS Workbench. The mode shapes of the shaft rotating at 10,000 rpm are almost identical to those of the stationary shaft; thus, they are omitted.

5.3 Modal Response of Long Shaft at Various Rotation Speeds

A Campbell diagram was generated for the long shaft using quadratic axisymmetric harmonic elements and results plotted against those of a three-dimensional solid element model in ANSYS Workbench. The operating speed evaluation points were 1 and 25,000 rpm (2,618 rad/s). The intersections of the natural frequency lines with the line having a slope of 1 are the predicted critical speeds. Since the excitation source of a rotor is often rotor imbalance causing one excitation per revolution of the shaft, critical speeds appear where operating speed is equivalent to a rotor natural frequency. Figure 5.9 displays the Campbell diagram.

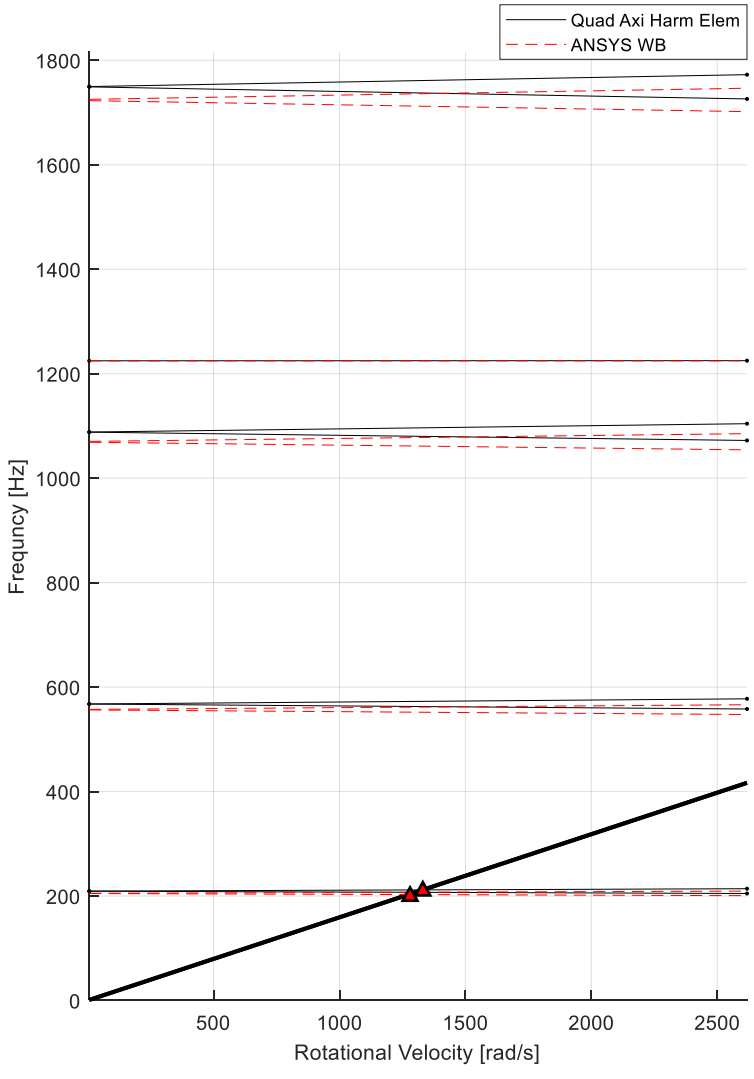

Figure 5.9: Campbell diagram comparison to ANSYS Workbench

The five modes that occur under 1,800 Hz are, in order, the first bend mode, the second bend mode, the third bend mode, the first mode having zero nodal waves (similar to that displayed in Figure 5.10), and the fourth bend mode.

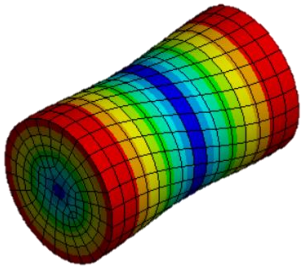

Figure 5.10: Mode shape of a shaft for the first mode having zero nodal waves

The divergence of the forward and backward whirl bend modes with increasing operating speed is observed. Critical speed predictions are seen as the *Frequency = Rotational Speed* line intersects the natural frequency lines. The Campbell diagram displays good agreement between the results of the quadratic axisymmetric harmonic elements and those of the three-dimensional solid element model in ANSYS Workbench.

When creating and interpreting a Campbell diagram in the design phase of turbomachinery, the analysis is performed from idle operating speed to above the 100% operating speed. For this example, the 100% operating speed is chosen as 2,000 rad/s. For safe machine operation, it is desired that no critical speeds are located within a certain range of 100% operating speed. For this example, it is desired that no critical speeds are within ±25% of 100% operating speed. These operating speeds are listed in appropriate units in Table 5.

Table 5: Operating speed range listed in several appropriate units

	100%	**75%**	**125%**
rpm	19,099	14,324	23,873
rad/s	20,000	15,000	25,000
Hz	318	239	390

Figure 5.11 shows the Campbell diagram with speed ranges and notations overlaid. The blue area depicts the 75%-125% operating speed range on the *x*-axis. The green areas depict the 75%-125% operating speed range on the *y*-axis. Where the two overlap (the yellow area), it is necessary that no natural frequency lines intersect the *Frequency = Rotational Speed* line ($y = 1 \cdot x$) resulting in a critical speed.

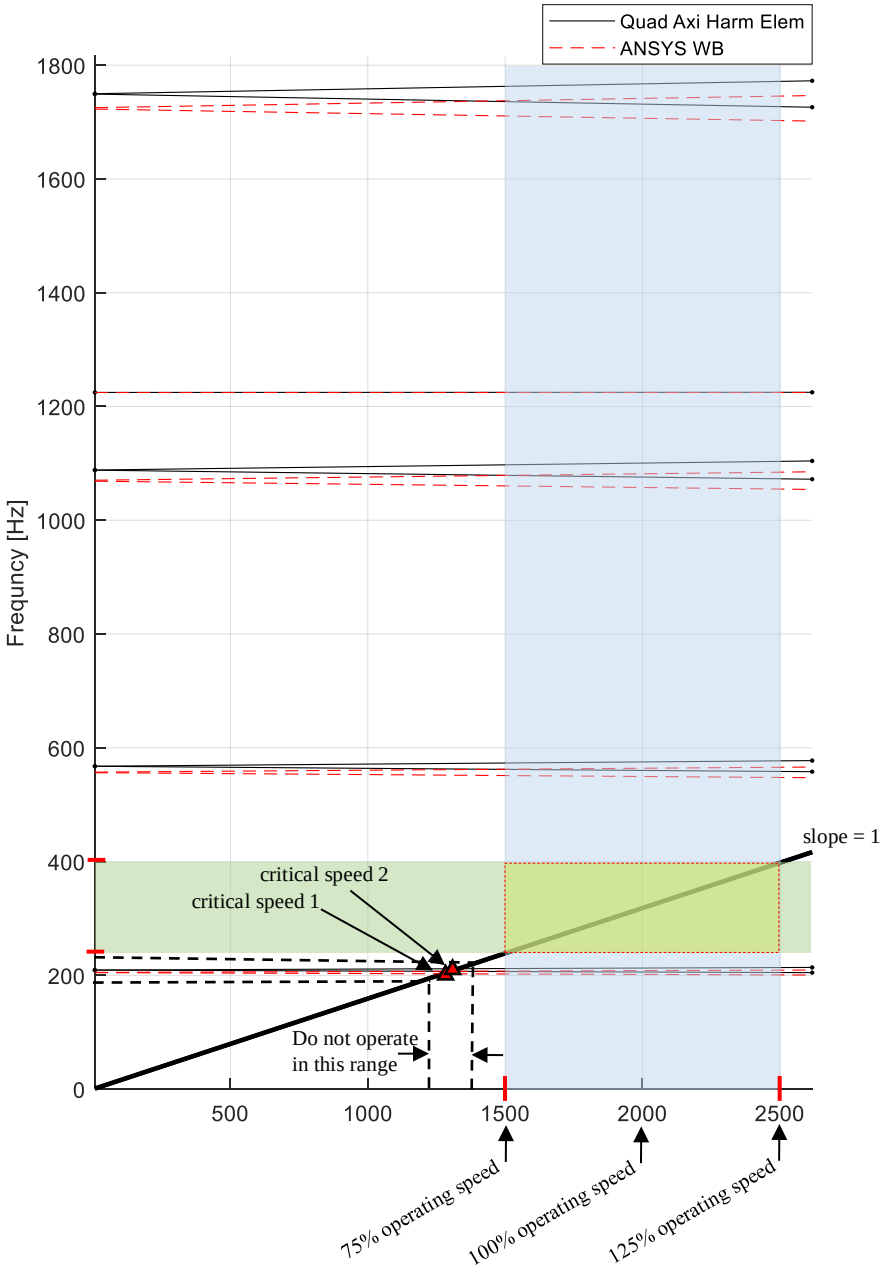

Figure 5.11: Campbell diagram with interpreting notation

The critical speeds of the rotating shaft are listed in Table 6.

Table 6: Critical speeds of rotating shaft

	Critical Speed 1	Critical Speed 2
rpm	12,166	12,433
rad/s	1274	1302
Hz	203	207

The Campbell diagram shows that there are two critical speeds that occur within the operating speed range analyzed. They are the backward and forward whirl first bend mode and occur at 203 and 207 Hz, respectively. Since these critical speeds are not within 75%-125% of the 100% operating speed, the present shaft design meets the design criterion. If, however, there were critical speeds in the ±25% of 100% operating speed range, the shaft would require design adjustments in order for its safe operation. Operating the turbomachinery at speeds near the critical speeds should be avoided, so the turbomachinery should pass quickly through the critical speed range (indicated by the black dashed lines on the Campbell diagram) while being brought up to 100% operating speed from its idle speed and vice-versa.

5.4 Modal Response of Long Shaft with Disk Model Rotating at 10,000 rpm

A modal analysis was performed for the long shaft with disk (model shaft 2). The mesh was generated using rectangular axisymmetric harmonic elements on a half-meridional cross-section of the shaft. The analysis was performed first using linear elements. The mesh using linear elements is shown in Figure 5.12.

Figure 5.12: Mesh of rotating long shaft with disk using linear elements

The analysis was performed again using quadratic elements. The mesh using quadratic elements is shown in Figure 5.13.

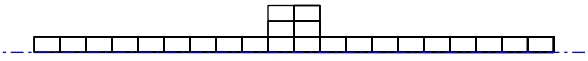

Figure 5.13: Mesh of rotating long shaft with disk using quadratic elements

The analysis was performed a third time using quadratic elements, but the disk geometry was omitted, and the material density of some elements was increased so that the mass of the shaft without the disk geometry included was equivalent to that of the shaft with the disk geometry included. This was done in the usual manner of equating the masses of the two geometric configurations and solving for the new density in terms of the other properties, which yielded:

$$\rho = \rho_0 \left(\frac{{r_{disk}}^2}{{r_{shaft}}^2} \right) = 7.07 \text{ x } 10^4 \text{ kg/m}^3 \qquad 5.1$$

The quadratic element mesh of the shaft omitting the disk geometry is shown in Figure 5.14.

Figure 5.14: Quadratic element mesh of the shaft omitting the disk geometry

A mesh convergence was performed for the analyses. Figure 5.15 displays the mesh convergence plots.

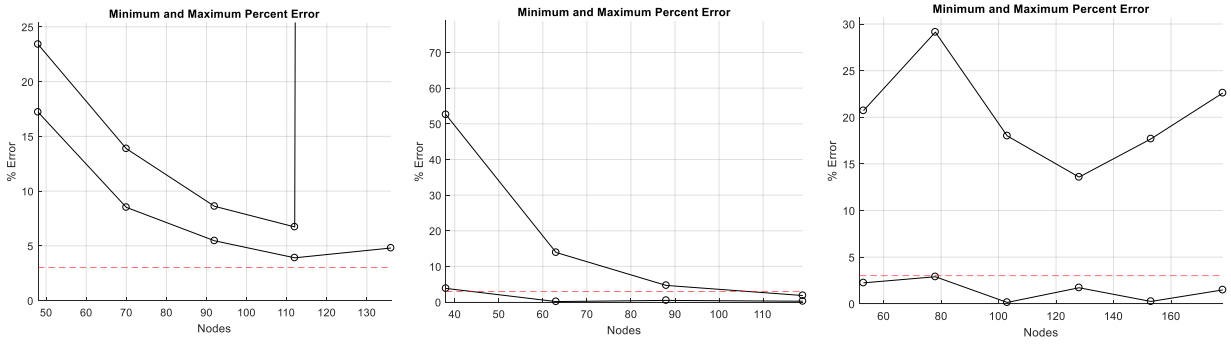

(a) **(b)** **(c)**

Figure 5.15: Model shaft 2 mesh convergence (a) linear, (b) quadratic, (c) quadratic (disk omitted)

The linear model converged to the criterion using 112 nodes (336 DOF). The quadratic model converged to the criterion using 119 nodes (357 DOF). The quadratic model omitting the disk geometry converged to the criterion using 128 nodes (384 DOF). The first four forward and backward whirl natural frequencies of the long shaft with disk and their associated percent errors against those calculated by commercial finite-element software are displayed in Table 7. Since there are no published results for this model shaft and operating speed, ANSYS Workbench is used as the benchmark.

Table 7: Comparison of natural frequencies for rotating long shaft with disk

Mode	**ANSYS WB**	**Disk Geometry Included**				**Disk Geometry Omitted (density adjusted)**	
		Linear		Quadratic		Quadratic	
1 BW	183	195	(6.07)	186	(1.53)	159	(-13.58)
1 FW	187	198	(5.98)	190	(1.52)	162	(-13.50)
2 BW	460	483	(4.99)	463	(0.72)	517	(12.55)
2 FW	551	573	(3.91)	553	(0.24)	538	(-2.43)
3 BW	982	1045	(6.38)	997	(1.56)	869	(-11.50)
3 FW	998	1061	(6.31)	1014	(1.56)	886	(-11.19)
4 BW	1269	1354	(6.73)	1292	(1.84)	1409	(11.03)
4 FW	1423	1502	(5.56)	1442	(1.30)	1448	(1.71)

The linear model consistently has approximately 4-7% error while the quadratic model has percent errors all under 2%. It is observed that in the model omitting the disk geometry and adjusting the material density the odd-numbered bend modes are consistently estimated at a lower natural frequency than the benchmark and that the even-numbered bend modes are consistently estimated at a higher natural frequency than the benchmark. Figure 5.16 displays this phenomenon.

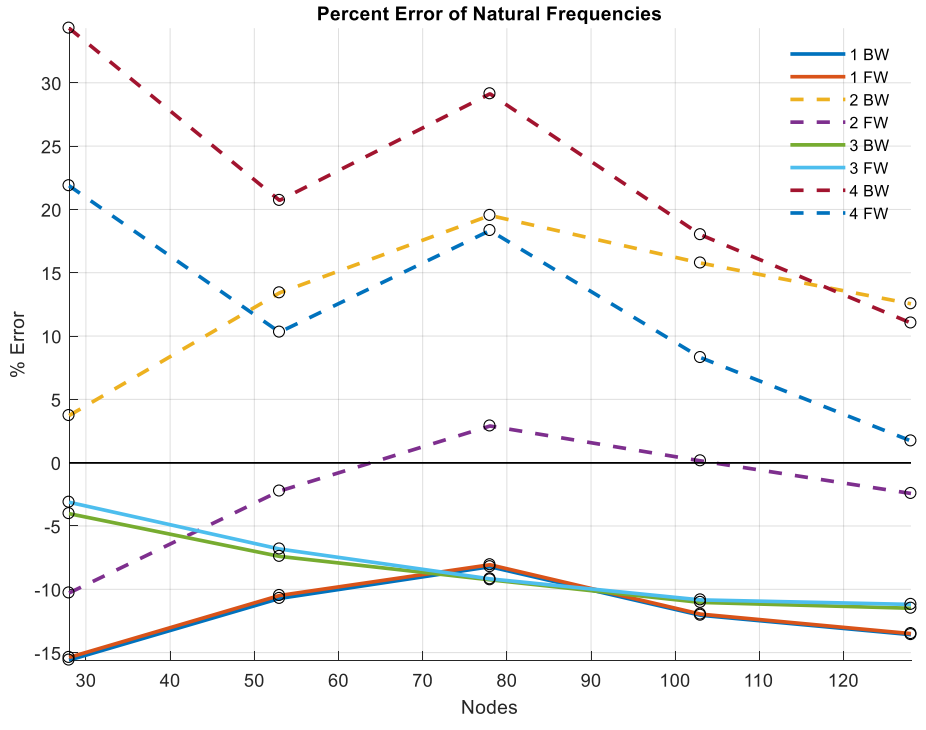

Figure 5.16: Natural frequency prediction behavior for odd- and even-numbered bend modes

The addition of the disk to model shaft 2 compared to model shaft 1 adds both mass and rotational inertia to the shaft. Modeling the disk geometry captures both the increase in mass and rotational inertia, but omitting the disk geometry while increasing material density to maintain total shaft mass captures only the increase in mass and not the increase in rotational inertia. This discrepancy in rotational inertia causes an increased error in natural frequency prediction. Compared to the long shaft without a disk (model shaft 1), the addition of a disk significantly changes the natural frequencies, but it does not add new mode shapes.

6 LIMITATIONS

This derivation only allows for the analysis of shafts having solid disks. In practice, most rotors have bladed disks, such as those found in gas turbine engines. Assuming the geometric dimensions (disk length and outer diameter) and material density of the solid disks are the same as those of the bladed disks, this means that the total mass of the modeled rotor using solid disks is greater than the total mass of the rotor using bladed disks. This discrepancy in mass creates a greater percent error in natural frequencies for models using solid disks. A model utilizing bladed disks would yield lower natural frequency percent errors than a model utilizing solid disks.

This derivation does not take into account the effect of bearing systems. In practice, rotors have a bearing system which affects its vibrational characteristics. While bearing properties did not need to be taken into account since the sample analyses all assumed a “free-free” rotor, a model which takes into account the stiffness and damping properties of the bearings of the rotor would yield natural frequencies and mode shapes more similar to those an actual rotor in an operating setting would display.

7 CONCLUSIONS

The present work gave a complete derivation for the mass, gyroscopic damping, and stiffness matrices and the dynamic equations of motion of the axisymmetric harmonic element using Hamilton's principle.

The formulation was applied to two different model shafts in four sample analyses. The rotor natural frequencies and mode shapes were attained by transforming the quadratic eigenvalue problem into a generalized eigenvalue problem. One analysis compared the natural frequencies of a uniform shaft without rotation to the results published by other authors. Another analysis compared the natural frequencies of a uniform shaft with rotation to those produced using commercial finite element software. The third analysis compared a Campbell diagram for a uniform shaft against that produced using commercial finite element software, and the final analysis compared the natural frequencies of a rotating shaft with disk against those calculated by commercial finite element software. All sample analyses verified the adequacy of the axisymmetric harmonic element formulation.

In view of the established objectives, this work expounded a clear and comprehensive presentation of all the steps of the finite element derivation for the modal analysis of a rotating axisymmetric structure, including gyroscopic effects. It bridged the gap between the derivations given in different works. Additionally, the method was made accessible to engineers having an introductory level of understanding in computational methods for structural dynamics. Lastly, the axisymmetric harmonic element was shown to predict with low percent error and few computational resources the natural frequencies of a rotor.

8 FUTURE WORK

The presentation of a method for modeling bladed disks while using axisymmetric harmonic elements other than using solid disks and a clear and comprehensive presentation of the derivation of general axisymmetric solid elements and cyclic symmetry in modal analyses are areas for future work. Additionally, the inclusion of bearing stiffness and damping properties into the calculation of natural frequencies and mode shapes would yield more realistic results.

LIST OF REFERENCES

[1] "Turbine operation," accessed August 10, 2019, https://commons.wikimedia.org/wiki/File:Turbofan_operation.png

[2] Swanson, E., Powell, C. D., Weissman, S., 2005, "A Practical Review of Rotating Machinery Critical Speeds and Modes," *Sound and Vibration*, Vol. 39, pp. 10-17

[3] Nelson, H. D., McVaugh, J. M., 1976, "The dynamics of rotor-bearing systems using finite elements, ASME *Journal of Engineering for Industry*, Vol. 98, pp. 593-600

[4] Geradin, M., and Kill, N., 1984, "A New Approach to Finite Element Modeling of Flexible Rotors," *Engineering Computations*, Vol. 1, pp. 52-64.

[5] Vance, J. M., Murphy, B. T., Tripp, H. A., 1987, "Critical Speeds of Turbomachinery: Computer Predictions vs. Experimental Measurements—Part I: The Rotor Mass—Elastic Model," ASME *Journal of Vibration, Acoustics, Stress, and Reliability in Design*, Vol. 109, pp. 1-7.

[6] Arora, R., 1987, "Axisymmetric finite elements for rotor dynamics," *M.S. Thesis, University of Kentucky*

[7] Stephenson, R. W., Rouch, K. E., Arora, R., 1989, "Modeling of Rotors with Axisymmetric Harmonic Elements," *Journal of Sound and Vibration*, Vol. 131, pp. 431-443

[8] Stephenson, R. W., Rouch, K. E., 1993, "Modeling Rotating Shafts Using Axisymmetric Solid Finite Elements with Matrix Reduction," ASME *Journal of Vibration and Acoustics*, Vol. 115, pp. 484-489

[9] Cook, R. D., Malkus, D. S., Plesha, M. E., Witt, R. J., *Concepts and Applications of Finite Element Analysis*, 4th ed. John Wiley & Sons, New York, 2001

[10] Singiresu S. Rao, *Vibration of Continuous Systems*, John Wiley & Sons, Hoboken, New Jersey, 2007

[11] *ANSYS Documentation, Mechanical APDL, Theory Reference, 17. Postprocessing, 17.15. POST1 – Modal Assurance Criterion (MAC). Release 17.1 - © SAS IP, Inc. All rights reserved.*

[12] Zienkiewicz, O.C., The Finite Element Method, 3rd ed., McGraw-Hill, London, 1977

APPENDICES

APPENDIX A

Gaussian Quadrature:

Table 8: Gauss points and weights

Number of points, n	Points, x_i	Weights, w_i
2	$\pm\sqrt{\frac{1}{3}}$	1
3	0	$\frac{8}{9}$
	$\pm\sqrt{\frac{3}{5}}$	$\frac{5}{9}$

$$\int_{-1}^{1}\int_{-1}^{1} f(s,t)\,ds\,dt \approx \sum_{i=1}^{n}\sum_{j=1}^{n} w_i w_j f(x_i, x_j)$$

APPENDIX B

Isoparametric Elements:

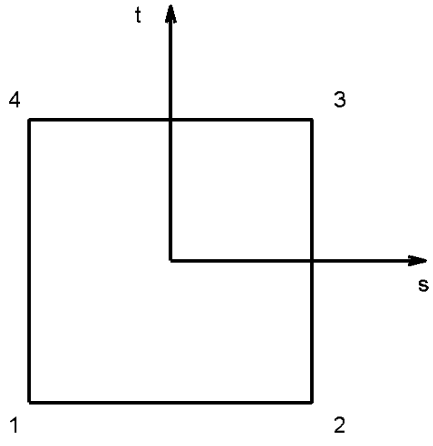

Figure B.1: 4-node isoparametric element

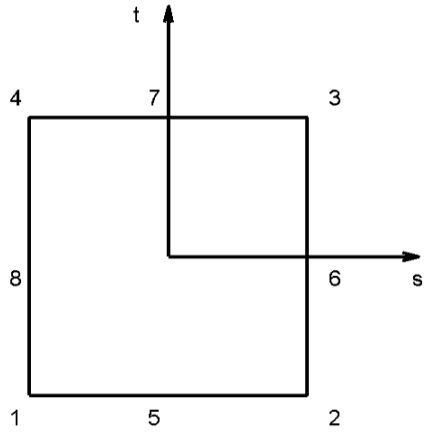

Figure B.2: 8-node isoparametric element

The linear shape functions are [12]:

$$N_1 = \frac{1}{4}(1-s)(1-t)$$

$$N_2 = \frac{1}{4}(1+s)(1-t)$$

$$N_3 = \frac{1}{4}(1+s)(1+t)$$

$$N_4 = \frac{1}{4}(1-s)(1+t)$$

The partial derivatives of the linear shape function with respect to *s* are:

$$\frac{dN_1}{ds} = -\frac{1}{4}(1-t)$$

$$\frac{dN_2}{ds} = \frac{1}{4}(1-t)$$

$$\frac{dN_3}{ds} = \frac{1}{4}(1+t)$$

$$\frac{dN_4}{ds} = -\frac{1}{4}(1+t)$$

The partial derivatives of the linear shape function with respect to *t* are:

$$\frac{dN_1}{dt} = -\frac{1}{4}(1-t)$$

$$\frac{dN_2}{dt} = -\frac{1}{4}(1+t)$$

$$\frac{dN_3}{dt} = \frac{1}{4}(1+t)$$

$$\frac{dN_4}{dt} = \frac{1}{4}(1-t)$$

The quadratic shape functions are:

$$N_1 = \frac{1}{4}(1-s)(1-t)(-s-t-1)$$

$$N_2 = \frac{1}{4}(1+s)(1-t)(\ \ s-t-1)$$

$$N_3 = \frac{1}{4}(1+s)(1+t)(\ \ s+t-1)$$

$$N_4 = \frac{1}{4}(1-s)(1+t)(-s+t-1)$$

$$N_5 = \frac{1}{2}(1-s^2)(1-t)$$

$$N_6 = \frac{1}{2}(1-t^2)(1+s)$$

$$N_7 = \frac{1}{2}(1-s^2)(1+t)$$

$$N_8 = \frac{1}{2}(1-t^2)(1-s)$$

The partial derivatives of the quadratic shape function with respect to *s* are:

$$\frac{\partial N_1}{\partial s} = -\frac{(t-1)(t+2s)}{4}$$

$$\frac{\partial N_2}{\partial s} = -\frac{(t-1)(-t+2s)}{4}$$

$$\frac{\partial N_3}{\partial s} = \frac{(1+t)(t+2s)}{4}$$

$$\frac{\partial N_4}{\partial s} = \frac{(1+t)(-t+2s)}{4}$$

$$\frac{\partial N_5}{\partial s} = s(t-1)$$

$$\frac{\partial N_6}{\partial s} = -\frac{(t^2-1)}{2}$$

$$\frac{\partial N_7}{\partial s} = -s(1+t)$$

$$\frac{\partial N_8}{\partial s} = \frac{(t^2-1)}{2}$$

The partial derivatives of the quadratic shape function with respect to *t* are:

$$\frac{\partial N_1}{\partial t} = -\frac{(s-1)(s+2t)}{4}$$

$$\frac{\partial N_2}{\partial t} = -\frac{(1+s)(s-2t)}{4}$$

$$\frac{\partial N_3}{\partial t} = \frac{(1+s)(s+2t)}{4}$$

$$\frac{\partial N_4}{\partial t} = \frac{(s-1)(s-2t)}{4}$$

$$\frac{\partial N_5}{\partial t} = \frac{(s^2-1)}{2}$$

$$\frac{\partial N_6}{\partial t} = -t(1+s)$$

$$\frac{\partial N_7}{\partial t} = -\frac{(s^2-1)}{2}$$

$$\frac{\partial N_8}{\partial t} = t(s-1)$$

APPENDIX C

The symmetric elemental mass matrix for a linear (4-node) element is:

$$[\bar{m}_e] = \rho \int [\bar{N}]^T [\bar{N}] dV$$

$$= \rho \int \begin{bmatrix}
N_1N_1cos^2\theta & 0 & 0 & N_1N_2cos^2\theta & 0 & 0 & N_1N_3cos^2\theta & 0 & 0 & N_1N_4cos^2\theta & 0 & 0 \\
0 & N_1N_1sin^2\theta & 0 & 0 & N_1N_2sin^2\theta & 0 & 0 & N_1N_3sin^2\theta & 0 & 0 & N_1N_4sin^2\theta & 0 \\
0 & 0 & N_1N_1cos^2\theta & 0 & 0 & N_1N_2cos^2\theta & 0 & 0 & N_1N_3cos^2\theta & 0 & 0 & N_1N_4cos^2\theta \\
N_2N_1cos^2\theta & 0 & 0 & N_2N_2cos^2\theta & 0 & 0 & N_2N_3cos^2\theta & 0 & 0 & N_2N_4cos^2\theta & 0 & 0 \\
0 & N_2N_1sin^2\theta & 0 & 0 & N_2N_2sin^2\theta & 0 & 0 & N_2N_3sin^2\theta & 0 & 0 & N_2N_4sin^2\theta & 0 \\
0 & 0 & N_2N_1cos^2\theta & 0 & 0 & N_2N_2cos^2\theta & 0 & 0 & N_2N_3cos^2\theta & 0 & 0 & N_2N_4cos^2\theta \\
N_3N_1cos^2\theta & 0 & 0 & N_3N_2cos^2\theta & 0 & 0 & N_3N_3cos^2\theta & 0 & 0 & N_3N_4cos^2\theta & 0 & 0 \\
0 & N_3N_1sin^2\theta & 0 & 0 & N_3N_2sin^2\theta & 0 & 0 & N_3N_3sin^2\theta & 0 & 0 & N_3N_4sin^2\theta & 0 \\
0 & 0 & N_3N_1cos^2\theta & 0 & 0 & N_3N_2cos^2\theta & 0 & 0 & N_3N_3cos^2\theta & 0 & 0 & N_3N_4cos^2\theta \\
N_4N_1cos^2\theta & 0 & 0 & N_4N_2cos^2\theta & 0 & 0 & N_4N_3cos^2\theta & 0 & 0 & N_4N_4cos^2\theta & 0 & 0 \\
0 & N_4N_1sin^2\theta & 0 & 0 & N_4N_2sin^2\theta & 0 & 0 & N_4N_3sin^2\theta & 0 & 0 & N_4N_4sin^2\theta & 0 \\
0 & 0 & N_4N_1cos^2\theta & 0 & 0 & N_4N_2cos^2\theta & 0 & 0 & N_4N_3cos^2\theta & 0 & 0 & N_4N_4cos^2\theta
\end{bmatrix} dV \qquad \text{C.1}$$

The antisymmetric elemental mass matrix for a linear (4-node) element is:

$$[\bar{\bar{m}}_e] = \rho \int [\bar{\bar{N}}]^T [\bar{\bar{N}}] dV$$

$$= \rho \int \begin{bmatrix}
N_1N_1sin^2\theta & 0 & 0 & N_1N_2sin^2\theta & 0 & 0 & N_1N_3sin^2\theta & 0 & 0 & N_1N_4sin^2\theta & 0 & 0 \\
0 & N_1N_1cos^2\theta & 0 & 0 & N_1N_2cos^2\theta & 0 & 0 & N_1N_3cos^2\theta & 0 & 0 & N_1N_4cos^2\theta & 0 \\
0 & 0 & N_1N_1sin^2\theta & 0 & 0 & N_1N_2sin^2\theta & 0 & 0 & N_1N_3sin^2\theta & 0 & 0 & N_1N_4sin^2\theta \\
N_2N_1sin^2\theta & 0 & 0 & N_2N_2sin^2\theta & 0 & 0 & N_2N_3sin^2\theta & 0 & 0 & N_2N_4sin^2\theta & 0 & 0 \\
0 & N_2N_1cos^2\theta & 0 & 0 & N_2N_2cos^2\theta & 0 & 0 & N_2N_3cos^2\theta & 0 & 0 & N_2N_4cos^2\theta & 0 \\
0 & 0 & N_2N_1sin^2\theta & 0 & 0 & N_2N_2sin^2\theta & 0 & 0 & N_2N_3sin^2\theta & 0 & 0 & N_2N_4sin^2\theta \\
N_3N_1sin^2\theta & 0 & 0 & N_3N_2sin^2\theta & 0 & 0 & N_3N_3sin^2\theta & 0 & 0 & N_3N_4sin^2\theta & 0 & 0 \\
0 & N_3N_1cos^2\theta & 0 & 0 & N_3N_2cos^2\theta & 0 & 0 & N_3N_3cos^2\theta & 0 & 0 & N_3N_4cos^2\theta & 0 \\
0 & 0 & N_3N_1sin^2\theta & 0 & 0 & N_3N_2sin^2\theta & 0 & 0 & N_3N_3sin^2\theta & 0 & 0 & N_3N_4sin^2\theta \\
N_4N_1sin^2\theta & 0 & 0 & N_4N_2sin^2\theta & 0 & 0 & N_4N_3sin^2\theta & 0 & 0 & N_4N_4sin^2\theta & 0 & 0 \\
0 & N_4N_1cos^2\theta & 0 & 0 & N_4N_2cos^2\theta & 0 & 0 & N_4N_3cos^2\theta & 0 & 0 & N_4N_4cos^2\theta & 0 \\
0 & 0 & N_4N_1sin^2\theta & 0 & 0 & N_4N_2sin^2\theta & 0 & 0 & N_4N_3sin^2\theta & 0 & 0 & N_4N_4sin^2\theta
\end{bmatrix} dV \qquad \text{C.2}$$

All entries of the elemental mass matrices contain either $cos^2\theta$ or $sin^2\theta$ terms. Integration can be carried out with respect to θ independently of the other coordinates [7] and upon noting that:

$$\int_0^{2\pi} cos^2\theta = \int_0^{2\pi} sin^2\theta = \pi \qquad \text{C.3}$$

The resulting mass matrix is of the form:

$$[\bar{m}_e] = [\bar{\bar{m}}_e] = [m_e] = \rho\pi \int_{-b}^{b} \int_{-a}^{a} [N]^T [N] r \, dr dz = \rho\pi \int_{-b}^{b} \int_{-a}^{a} [m] r \, dr dz \qquad \text{C.4}$$

where:

C.5

$$[m] = \begin{bmatrix} N_1N_1 & 0 & 0 & N_1N_2 & 0 & 0 & N_1N_3 & 0 & 0 & N_1N_4 & 0 & 0 \\ 0 & N_1N_1 & 0 & 0 & N_1N_2 & 0 & 0 & N_1N_3 & 0 & 0 & N_1N_4 & 0 \\ 0 & 0 & N_1N_1 & 0 & 0 & N_1N_2 & 0 & 0 & N_1N_3 & 0 & 0 & 0 \\ N_2N_1 & 0 & 0 & N_2N_2 & 0 & 0 & N_2N_3 & 0 & 0 & N_2N_4 & 0 & 0 \\ 0 & N_2N_1 & 0 & 0 & N_2N_2 & 0 & 0 & N_2N_3 & 0 & 0 & N_2N_4 & 0 \\ 0 & 0 & N_2N_1 & 0 & 0 & N_2N_2 & 0 & 0 & N_2N_3 & 0 & 0 & N_2N_4 \\ N_3N_1 & 0 & 0 & N_3N_2 & 0 & 0 & N_3N_3 & 0 & 0 & N_3N_4 & 0 & 0 \\ 0 & N_3N_1 & 0 & 0 & N_3N_2 & 0 & 0 & N_3N_3 & 0 & 0 & N_3N_4 & 0 \\ 0 & 0 & N_3N_1 & 0 & 0 & N_3N_2 & 0 & 0 & N_3N_3 & 0 & 0 & N_3N_4 \\ N_4N_1 & 0 & 0 & N_4N_2 & 0 & 0 & N_4N_3 & 0 & 0 & N_4N_4 & 0 & 0 \\ 0 & N_4N_1 & 0 & 0 & N_4N_2 & 0 & 0 & N_4N_3 & 0 & 0 & N_4N_4 & 0 \\ 0 & 0 & N_4N_1 & 0 & 0 & N_4N_2 & 0 & 0 & N_4N_3 & 0 & 0 & N_4N_4 \end{bmatrix}$$

In similar fashion, the element stiffness matrices for nodal wave number $n = 1$ contain $cos^2\theta$ or $sin^2\theta$ in every term. These matrices simplify to:

$$\left[\bar{k}_e\right] = \left[\bar{\bar{k}}_e\right] = [k_e] = \pi \int_{-b}^{b} \int_{-a}^{a} [B]^T [E][B] r \, dr dz \qquad \text{C.6}$$

APPENDIX D

The discretized form of the kinetic energy due to gyroscopic effects is:

$$T_g = \Omega \int \left(\frac{\partial \dot{\bar{v}}}{\partial z} \bar{\bar{w}} + \frac{\partial \dot{\bar{\bar{v}}}}{\partial z} \bar{w} \right) r dm = \Omega \int D r dm \qquad \text{D.1}$$

The term *D* in Equation D.1 can be written as:

$$D = \left\{ \dot{\bar{d}} \right\}^T \left[\frac{\partial \bar{N}_\theta}{\partial z} \right]^T \left[\bar{\bar{N}}_z \right] \{ \bar{\bar{d}} \} + \left\{ \dot{\bar{\bar{d}}} \right\}^T \left[\frac{\partial \bar{\bar{N}}_\theta}{\partial z} \right]^T \left[\bar{N}_z \right] \{ \bar{d} \} = \{ \dot{d} \}^T [C] \{ d \} \qquad \text{D.2}$$

$[C]$ is a *3N* x *3N* matrix containing $2N^2$ non-zero terms. Indices of $[C]$ have the form:

$$c_{kl} = \frac{\partial N_i}{\partial z} N_j \qquad\qquad c_{lk} = \frac{\partial N_i}{\partial z} N_j \qquad \text{D.3}$$

k and l are:

$$k = 3(i-1) + 2 \qquad\qquad l = 3(j-1) + 3 \qquad \text{D.4}$$

For $i = 1,2, \dots, N$ and $j = 1,2, \dots, N$.

The elemental gyroscopic damping matrix in integral form is [8]:

$$[c_e] = \pi \Omega \int [C] \rho r^2 dr dz \qquad \text{D.5}$$

Where $[C]$ has the form:

$$[C] = \begin{bmatrix} [C_{1,1}] & [C_{1,2}] & \dots & [C_{1,N}] \\ [C_{2,1}] & [C_{2,2}] & \dots & [C_{2,N}] \\ \vdots & \vdots & \dots & \vdots \\ [C_{N,1}] & [C_{N,2}] & \dots & [C_{N,N}] \end{bmatrix} \qquad \text{D.6}$$

And submatrices $[C_{i,j}]$ are of the form:

$$\left[C_{i,j}\right] = \begin{bmatrix} 0 & 0 & 0 \\ 0 & 0 & \dfrac{\partial N_i}{\partial z} N_j \\ 0 & \dfrac{\partial N_j}{\partial z} N_i & 0 \end{bmatrix} \tag{D.7}$$

For clarity and insight, the gyroscopic damping matrix for a linear element is given.

$$[C] = \begin{bmatrix}
0 & 0 & 0 & 0 & 0 & 0 & 0 & 0 & 0 & 0 & 0 & 0 \\
0 & 0 & \dfrac{\partial N_1}{\partial z} N_1 & 0 & 0 & \dfrac{\partial N_1}{\partial z} N_2 & 0 & 0 & \dfrac{\partial N_1}{\partial z} N_3 & 0 & 0 & \dfrac{\partial N_1}{\partial z} N_4 \\
0 & \dfrac{\partial N_1}{\partial z} N_1 & 0 & 0 & \dfrac{\partial N_2}{\partial z} N_1 & 0 & 0 & \dfrac{\partial N_3}{\partial z} N_1 & 0 & 0 & \dfrac{\partial N_4}{\partial z} N_1 & 0 \\
0 & 0 & 0 & 0 & 0 & 0 & 0 & 0 & 0 & 0 & 0 & 0 \\
0 & 0 & \dfrac{\partial N_2}{\partial z} N_1 & 0 & 0 & \dfrac{\partial N_2}{\partial z} N_2 & 0 & 0 & \dfrac{\partial N_2}{\partial z} N_3 & 0 & 0 & \dfrac{\partial N_2}{\partial z} N_4 \\
0 & \dfrac{\partial N_1}{\partial z} N_2 & 0 & 0 & \dfrac{\partial N_2}{\partial z} N_2 & 0 & 0 & \dfrac{\partial N_3}{\partial z} N_2 & 0 & 0 & \dfrac{\partial N_4}{\partial z} N_2 & 0 \\
0 & 0 & 0 & 0 & 0 & 0 & 0 & 0 & 0 & 0 & 0 & 0 \\
0 & 0 & \dfrac{\partial N_3}{\partial z} N_1 & 0 & 0 & \dfrac{\partial N_3}{\partial z} N_2 & 0 & 0 & \dfrac{\partial N_3}{\partial z} N_3 & 0 & 0 & \dfrac{\partial N_3}{\partial z} N_4 \\
0 & \dfrac{\partial N_1}{\partial z} N_3 & 0 & 0 & \dfrac{\partial N_2}{\partial z} N_3 & 0 & 0 & \dfrac{\partial N_3}{\partial z} N_3 & 0 & 0 & \dfrac{\partial N_4}{\partial z} N_3 & 0 \\
0 & 0 & 0 & 0 & 0 & 0 & 0 & 0 & 0 & 0 & 0 & 0 \\
0 & 0 & \dfrac{\partial N_4}{\partial z} N_1 & 0 & 0 & \dfrac{\partial N_4}{\partial z} N_2 & 0 & 0 & \dfrac{\partial N_4}{\partial z} N_3 & 0 & 0 & \dfrac{\partial N_4}{\partial z} N_4 \\
0 & \dfrac{\partial N_1}{\partial z} N_4 & 0 & 0 & \dfrac{\partial N_2}{\partial z} N_4 & 0 & 0 & \dfrac{\partial N_3}{\partial z} N_4 & 0 & 0 & \dfrac{\partial N_4}{\partial z} N_4 & 0
\end{bmatrix} \tag{D.8}$$